A Numerical Study of Vortices and Turbulence in Ultra-cold Bose Gases and Superfluid Helium

George William Stagg

Thesis submitted for the degree of
Doctor of Philosophy

School of Mathematics & Statistics
Newcastle University
Newcastle upon Tyne
United Kingdom

June 2016

Acknowledgements

I would like to thank everybody…

Abstract

Insert your abstract here.

Contents

Part I

Introduction

Chapter 1

Introduction to Bose-Einstein Condensates

1.1 Superfluid Helium

1.2 Ultra-cold Bose Gases

1.3 Bose-Einstein Condensation

1.4 Macroscopic excitations: Vortices and Solitons

Chapter 2

Theoretical Modeling of BEC

2.1 Mean-field description

We aim to accurately model the dynamics of a closed system containing a dilute, weakly interacting Bose gas of N atoms, at extremely low temperatures. One could model the entire system by constructing a N-body quantum wavefunction, which would follow the Schrödinger equation, but the complexity of this method makes it extremely unwieldy to model the large number of particles used in Bose-Einstein condensate (BEC) experiments happening all around the world.

We instead model the system with a mean-field theory, in which there are essentially two main approximations. Firstly, justified by the dilute property of the gas, any binary interaction between particles is assumed to be a contact delta function,

$$V(\mathbf{r} - \mathbf{r}') = g\delta(\mathbf{r} - \mathbf{r}').$$

Interactions involving a higher number of particles are ignored. Secondly, we assume all particles in the condensate are macroscopically described by a single wavefunction, $\psi(\mathbf{r}, t)$. As the particles all share the same phase and quantum state, $\psi(\mathbf{r}, t)$ is a classical field. This second approximation also assumes that there are no particles contributing to thermal or quantum fluctuations beyond the classical field, and so is only strictly justified when the temperature, T, is exactly 0K.

2.2 The Gross-Pitaevskii Equation

The result of this methodology is the Gross-Pitaevskii equation (GPE),

$$i\hbar \frac{\partial \Psi(\mathbf{r}, t)}{\partial t} = \left(-\frac{\hbar^2}{2m} \nabla^2 + V(\mathbf{r}, t) + g|\Psi(\mathbf{r}, t)|^2 - \mu \right) \Psi(\mathbf{r}, t), \tag{2.1}$$

where $V(\mathbf{r}, t) = V_{\text{obj}}(\mathbf{r}, t) + V_{\text{trap}}(\mathbf{r}, t)$. When trapped, the trap is harmonic and of the form $V_{\text{trap}}(\mathbf{r}, t) = m\omega^2 r^2/2$, otherwise $V_{\text{trap}}(\mathbf{r}, t) = 0$.

Taking into account the fact that the GPE is only valid at $T = 0$, it turns out the equation is surprisingly successful at quantitatively modelling ultra-cold gasses, even up to a temperature of $T = \frac{T_c}{2}$, where T_c is the critical temperature for Bose-Einstein condensation. The GPE is also successful at qualitatively modelling BEC based effects in higher temperature superfluids, such as liquid helium II.

A detailed explanation of the mean-field formulation of the model and the full derivation of the GPE is shown in Section A.3.

2.3 Quasi-Two-Dimensional Gross-Pitaevskii Equation

When $\omega_z >> \omega_r$ and $\hbar\omega_z >> \mu$ the condensate becomes highly oblate. Tight z confinement causes the dynamics to become essentially two dimensional. In this case a 2DGPE can be used to model the system where $g_{2D} = g/\left(\sqrt{2\pi} l_z\right)$. [CITE PARKER THESIS] The chemical potential is also modified. See Section 2.5.2 for details on μ.

To effectively reduce the system to two-dimensions, the BEC is assumed to be confined by a harmonic trapping potential in the axial (z) direction, $V(z) = \frac{1}{2} m\omega_z^2 z^2$, where m is the atomic mass. For sufficiently strong trapping, which requires $\hbar\omega_z \gg \mu$, where μ is the chemical potential of the 3D condensate, the axial wavefunction becomes “frozen" into the time-independent harmonic oscillator ground state $\pi^{-1/4} l_z^{-1/2} \exp\left(-z^2/2l_z^2\right)$, where $l_z = \sqrt{\hbar/m\omega_z}$ is the axial harmonic oscillator length. Under these conditions, the condensate becomes effectively two-dimensional, as achieved experimentally [1]. It is then described by an 2D GPE, corresponding to Equation (8.1) with $g \to g/2\pi l_z^2$ and where Ψ, $\mathbf{r}$, V and n become two-dimensional quantities.

2.4 Dimensionless Gross-Pitaevskii Equations

Bose-Einstein condensates can be formed with almost any size or scale. An ultra-cold BECs topology or atom interaction strength can be fairly easily changed with magnetic/optical potentials and Feshbach resonances. Superfluid helium can have vortex core sizes of ~1 or ~100 angstroms, depending on the isotope of helium used. The cores of neutron stars are even theorised to be superfluid. For this reason, it is desirable to rescale the length scales used in the GPE so that any of the calculations performed can be easily reformulated into any length scale desired. We make this process easier by doing all calculations with dimensionless parameters.

2.4.1 Homogeneous GPE

When discussing a homogeneous condensate we drop the dimensionless modifiers for each quantity and use the equation,

$$\mathrm{i}\frac{\partial\psi(\mathbf{r},t)}{\partial t} = \left(-\frac{1}{2}\nabla^2 + |\psi(\mathbf{r},t)|^2 + V_{\mathrm{obj}}(\mathbf{r},t) - 1\right)\psi(\mathbf{r},t). \tag{2.2}$$

2.4.2 Trapped GPE

When discussing the a trapped condensate we drop the dimensionless modifiers for each quantity and use the equation,

$$\mathrm{i}\frac{\partial\phi(\mathbf{r},t)}{\partial t} = \left(-\frac{1}{2}\nabla^2 + g|\phi(\mathbf{r},t)|^2 + V(\mathbf{r},t) - 1\right)\phi(\mathbf{r},t). \tag{2.3}$$

Where $V(\mathbf{r},t) = \frac{r^2}{2} + V_{\mathrm{obj}}(\mathbf{r},t)$

2.5 The Dissipative Gross-Pitaevskii Equation

2.5.1 Phenomenological dissipation

The GPE can be modified to provide a simple phenomenological model of a condensate's interaction with the thermal cloud. The phenomenological damping term, γ, is added to the right hand side of the GPE with the effect that the energy in the system no longer remains constant. The energy will instead vary over time to approach some constant value. This has the effect of damping out any excitations made to the condensate, and over time the wavefunction approaches the steady state. A microscopic justification for this model was provided by Penckwitt et al [CITE] and Gardiner at al [CITE]; by studying the growth of a condensate in the presence of a rotating thermal cloud an expression for γ was found.

$$\gamma = \frac{4m\tilde{g}a^2kT}{\pi\hbar^2} \approx 0.01, \tag{2.4}$$

where k is Boltzmann's constant and $\tilde{g} = 3$ is a factor used for correction. As γ is proportional to temperature, in this thesis various values of γ will be used as a qualitative probe of finite-temperature dynamics with only marginally more complex numerical methods. In the case with a homogeneous condensate this leaves us with

$$(\mathrm{i}-\gamma)\frac{\partial\psi(\mathbf{r},t)}{\partial t} = \left(-\frac{1}{2}\nabla^2 + |\psi(\mathbf{r},t)|^2 + V_{\mathrm{obj}}(\mathbf{r},t) - 1\right)\psi(\mathbf{r},t), \tag{2.5}$$

and in the case with a trapped condensate this leaves us with

$$(\mathrm{i}-\gamma)\frac{\partial\phi(\mathbf{r},t)}{\partial t} = \left(-\frac{1}{2}\nabla^2 + g|\phi(\mathbf{r},t)|^2 + V(\mathbf{r},t) - 1\right)\phi(\mathbf{r},t). \tag{2.6}$$

2.5.2 The role of the chemical potential

2.6 Hydrodynamic interpretation

Often it can be helpful to write the GPE, via the so called Madelung transformation, as a set of hydrodynamic equations. The transformation reinterprets the wavefunction Ψ as a magnitude directly related to the fluid density and a phase which is directly related to the fluid velocity. We write the wavefunction in the form

$$\Psi(\mathbf{r},t) = R(\mathbf{r},t)\exp(\mathrm{i}\theta(\mathbf{r},t)), \tag{2.7}$$

and identify the fluid density as $\rho = mR^2$ and the velocity as $\mathbf{v} = \frac{\hbar}{m}\nabla\theta$. In vector form we obtain a continuity equation

$$\frac{\partial\rho}{\partial t} + \nabla(\rho\mathbf{v}) = 0, \tag{2.8}$$

and an equation similar to the Euler equation for an inviscid fluid,

$$\rho\left(\frac{\partial\mathbf{v}}{\partial t} + (\mathbf{v}\cdot\nabla)\,\mathbf{v}\right) = -\nabla p - \nabla\mathbf{P} - \rho\nabla\left(\frac{V}{m}\right). \tag{2.9}$$

where $P_{jk} = -\frac{\hbar^2}{4m^2}\rho\frac{\partial^2\ln\rho}{\partial x_j\partial x_k}$. A detailed derivation of this result can be found in Appendix A.2.

2.7 A selection of analytical solutions

2.7.1 Density near a wall

2.7.2 Soliton solutions

$$\Psi(x) = \Psi_0\tanh\left(\frac{x}{\sqrt{2}\xi}\right) \tag{2.10}$$

2.7.3 A note on vortex solutions

2.8 Initial Conditions

2.8.1 Thomas Fermi profile of a trapped condensate

Fixed in time Ψ and V.

$$\sqrt{\frac{\mu - V(\mathbf{r})}{g}} = \Psi(\mathbf{r}) \tag{2.11}$$

2.8.2 Classical Field approximation with a homogeneous condensate

$$\psi(\mathbf{r}, t) = \sum_{\mathbf{k}} a_{\mathbf{k}} \exp(\mathrm{i}\mathbf{k} \cdot \mathbf{r}), \tag{2.12}$$

where the complex Fourier amplitudes $a_{\mathbf{k}}$ are related to the occupation numbers $n_{\mathbf{k}}$ through $\langle a_{\mathbf{k}} a^*_{\mathbf{k}'} \rangle = n_{\mathbf{k}} \delta_{\mathbf{k}\mathbf{k}'}$. The phase of the complex amplitudes $a_{\mathbf{k}}$ are distributed uniformly on $[0, 2\pi]$ while $|a_{\mathbf{k}}|$ is distributed randomly with fixed mean equal to unity; it has been found that different distributions of $|a_{\mathbf{k}}|$ make no qualitative difference to the turbulent evolution[phys rev A 66 013603]. [TODO: write about choice of E and N here to get different condensate fractions]

We also have the integral distribution function,

$$D_k = \sum_{k' < k} n_{\mathbf{k}}. \tag{2.13}$$

This is a coarse-grained characteristic of the particle distribution which shows how many particles have momenta less than k.

2.9 Creating obstacles with repulsive potentials

2.9.1 Three-dimensional elliptical Gaussian

In our 3D simulations, we solve the 3D GPE of Equation (1), where the localized 3D obstacle is modelled via a repulsive ellipsoidal Gaussian potential,

$$V(\mathbf{r}, t) = V_0 \exp\left(-\frac{\varepsilon^2 (x - x_0 - vt)^2}{d^2} - \frac{(y - y_0)^2}{d^2} - \frac{(z - z_0)^2}{d^2} \right), \tag{2.14}$$

where V_0 is its (constant) amplitude, d its width in the y and z directions, and (x_0, y_0, z_0) its initial coordinates.

2.9.2 Three-dimensional cylindrical Gaussian

2.9.3 Three-dimensional 'realistic rough-surface'

2.9.4 Two-dimensional Gaussian

In 2D, we model the obstacle via a moving repulsive Gaussian potential of the form,

$$V(\mathbf{r}, t) = V_0 \exp\left(-\frac{\varepsilon^2(x - x_0 - vt)^2}{d^2} - \frac{(y - y_0)^2}{d^2}\right). \tag{2.15}$$

2.9.5 Two-dimensional arbitrary bitmap

2.10 An alternative reference frame

The GPE is transformed into the reference frame moving with the obstacle (in x) via the addition of the Galilean term $i\hbar v \frac{\partial}{\partial x}\Psi$ to the right-hand side of the GPE (8.1), where v is the frame velocity.

Part II

Numerical Methods

Chapter 3

Numerical Methods

3.1 Numerical procedures for 2D and 3D solutions

3.1.1 Fourth order Runge-Kutta scheme

The classical fourth-order Runge-Kutta formula (RK4) is described equivalently in many texts. We follow the description in [2]. Let an initial value problem be specified as

$$\frac{\partial \psi}{\partial t} = f(\psi, t), \qquad \psi(t_0) = \psi_0.$$

A step-size, $h > 0$, is chosen as the parameter controlling how the solution is advanced over t. The scheme for estimating $\psi(t_n) = \psi_n$ is then written

$$\begin{aligned} k_1 &= hf(t_n, \psi_n), \\ k_2 &= hf(t_n + \frac{h}{2}, \psi_n + \frac{k_1}{2}), \\ k_3 &= hf(t_n + \frac{h}{2}, \psi_n + \frac{k_2}{2}), \\ k_4 &= hf(t_n + h, \psi_n + k_3), \\ \psi_{n+1} &= \psi_n + \frac{k_1}{6} + \frac{k_2}{3} + \frac{k_3}{3} + \frac{k_4}{6} + O(h^5), \\ t_{n+1} &= t_n + h. \end{aligned} \tag{3.1}$$

A full derivation and proof of accuracy for the RK4 scheme is outlined in Appendix A.1.

```
input  : A field n_x × n_y P, A function f, a step size h, current time t
repeat
    k_1 ← f(P, t);
    for i ← 1 to n_x do
        for j ← 1 to n_y do
            R[i, j] ← P[i, j] + (h/2) k_1[i, j];
        end
    end
    k_2 ← f(R, t + h/2);
    for i ← 1 to n_x do
        for j ← 1 to n_y do
            R[i, j] ← P[i, j] + (h/2) k_2[i, j];
        end
    end
    k_3 ← f(R, t + h/2);
    for i ← 1 to n_x do
        for j ← 1 to n_y do
            R[i, j] ← P[i, j] + h k_3[i, j];
        end
    end
    k_4 ← f(R, t + h);
    for i ← 1 to n_x do
        for j ← 1 to n_y do
            P[i, j] ← (h/6)(k_1[i, j] + 2k_2[i, j] + 2k_3[i, j] + k_4[i, j]);
        end
    end
    t ← t + h;
    if normalization is enabled then
        N ← norm(P);
        for i ← 1 to n_x do
            for j ← 1 to n_y do
                P[i, j] ← P[i, j]/√N;
            end
        end
    end
until satisfied;
```

Algorithm 1: RK4 algorithm for advancing a ODE/PDE in time. Should normalization of the be required it is included an optional part of this algorithm.

In all of our relevant calculations the value of f is set as the right hand side of the homogeneous or trapped GPE. The main loop formulating the RK4 method may be repeated indefinitely to reach any $t > t_0$. The step size for a given set of parameters should be chosen small enough that smaller choices make no quantitative changes to the resulting solution.

3.1.2 Obtaining the ground-state with imaginary time

Many explorations in quantum systems, particularly those associated with magnetic or optical trapping, involve calculating the ground-state, the lowest-lying eigenvalue along with its eigenfunction, as either the final result or as a stepping stone for further calculations. Complications arise in calculating the ground-state in the case of the GPE; the non-linearity of the system forces the true ground-state to solve many linear eigenvalue problems as a collection. This complex problem is therefore often solved numerically using so called eigensolvers. There are several methods available for implementing a numerical eigensolver including but not limited to: inverse iteration and Lanczos methods [CITE], systematic variational techniques [CITE], boundary eigenvalue methods [CITE], conjugate gradient techniques [CITE] and imaginary time propagation [CITE]. We choose to use the last of these methods due to its relative simplicity at the expense of computational time.

The method revolves around moving from real to imaginary time using a Wick rotation $\tau = it$. [IMAGE: Energy of trapped system as imaginary time is run - compare with TF energy] [IMAGE: ground state as found by imaginary time]

3.1.3 Numerical stability

We now systematically study the numerical stability of common simulated systems. Our aim is to find a suitable discretisaton of space and time so that while simulations are timely, our numerical solutions are converged and not overly sensitive to small changes computational parameters.

We use energy to measure because in the undamped gpe energy is conserved.

We run 100 units of imaginary time stepping to get density profile We run another 100 units for vortex IC We run 500 units in real time to study stability

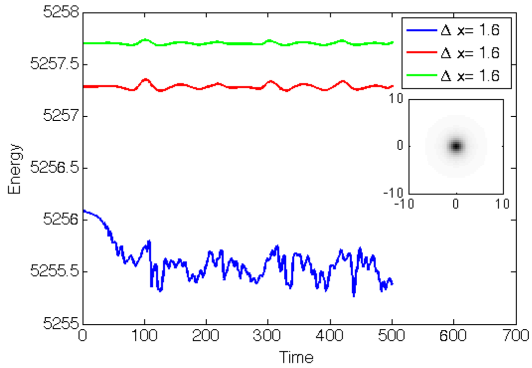

3.2 Identifying vortices

input : A $n_x \times n_y$ field θ. A $n_x \times n_y$ field P. A line integral width l.
output: A $n_x \times n_y$ field Q.

for $i \leftarrow 1 + l/2$ **to** $n_x - l/2$ **do**
  for $i \leftarrow 1 + l/2$ **to** $n_y - l/2$ **do**
    $Q[i, j] \leftarrow \oint_\square \nabla\theta \, ds$, where $\square$ is a square loop of width l centered on (i, j);
  end
  if $P[i, j] > 1$ **then** $Q[i, j] \leftarrow 0$;
end

Algorithm 2: Initial vortex detection. Outputs a field with positive values near a vortex with circulation 1, negative values near a vortex with circulation -1 and zero valued otherwise.

```
input  : A n_x × n_y binary field P.
output : A n_x × n_y field Q.

Let linked be a (n_x.n_y) × 4 field;
linked ← −1 at every point, Q ← −1 at every point;
lc ← 1, rc ← 0;
for i ← 2 to n_x − 1 do
    for j ← 2 to n_y − 1 do
        if P[i, j] = 0 then skip this loop iteration;
        foreach c ∈ (Q[i + 1, j − 1], Q[i, j − 1], Q[i − 1, j − 1], Q[i − 1, j]) do
            if c ≥ 0 then
                Q[i, j] ←c;
                linked[lc , 1] ←c;
            end
        end
        if Q[i, j] ≥ 0 then lc ←lc +1;
        else
            Q[i,j]←rc;
            rc ←rc +1;
        end
    end
end
for i ← 1 to (n_x × n_y) do
    if max(All elements of linked from row i)= −1 then continue;
    m ← min(All elements of linked from row i with value≥ 0);
    for j ← 1 to 4 do
        if linked[i, j] ≠ m and linked[i, j] ≥ 0 then
            for k ← 1 to n_x do
                for l ← 1 to n_y do
                    if Q[k, l] = linked[i, j] then Q[k, l] = m;
                end
            end
        end
    end
end
```

Algorithm 3: The B/W Label algorithm. Outputs a field with the same non-zero regions of the input binary field, but with each connected region labeled with a unique value.

3.2.1 Image filters and the Gaussian kernel

input : A $n_x \times n_y$ field P, a Gaussian filter width g.
output: A $n_x \times n_y$ field Q.

$Q \leftarrow 0$ at every point;
for $k \leftarrow 1$ **to** n_x **do**
  for $l \leftarrow 1$ **to** n_y **do**
    for $i \leftarrow 1$ **to** n_x **do**
      for $j \leftarrow 1$ **to** n_y **do**
        $Q[k, l] \leftarrow Q[k, l] + P[i, j] \times \exp\left(-[(k-i)^2 + (l-j)^2]/g^2\right)$;
      end
    end
    $Q[k, l] \leftarrow Q[k, l]/(n_x \times n_y)$;
  end
end

Algorithm 4: Gaussian convolution. Filters out features with structures of size less than the input filter width. The output is analagous to a 'blurring' of the input field. This allows high frequency noise to be removed.

input : A $n_x \times n_y$ field θ. A $n_x \times n_y$ field P. A threshold value t.
output : Number of vortices found, n_v. Vortex location, a $2 \times n_v$ field V_l. Vortex polarity, a vector V_p of length n_v.

$Q \leftarrow$ Algorithm 4 $\leftarrow$ Algorithm 2 $\leftarrow (\theta, P)$;
$R \leftarrow 0$ at every point, $S \leftarrow 0$ at every point;
$n_v \leftarrow 0$;
for $i \leftarrow 1$ **to** n_x **do**
    for $j \leftarrow 1$ **to** n_y **do**
        if $Q[i, j] > t$ **then** $R[i, j] = 1$;
        if $Q[i, j] < t$ **then** $S[i, j] = 1$;
    end
end
foreach $C \in (R, S)$ **do**
    $D \leftarrow$ Algorithm 3 $\leftarrow C$;
    for $i \leftarrow 1$ **to** `max` (D) **do**
        $V[1, n_v] \leftarrow$ mean row of the points where $D = i$;
        $V[2, n_v] \leftarrow$ mean column of the points where $D = i$;
        if $C = R$ **then** $V[3, n_v] \leftarrow 1$;
        if $C = S$ **then** $V[3, n_v] \leftarrow -1$;
        $n_v \leftarrow n_v + 1$;
    end
end

Algorithm 5: Calculate vortex locations and polarity.

3.3 Quantifying vortex clustering

3.3.1 Recursive Cluster Algorithm (RCA)

input : Vortex location, a $2 \times n_v$ field V_l. Vortex polarity, a vector V_p of length n_v. Number of vortices, n_v.

output : Vortex decomposition, a vector V_{rca} of length n_v.

$n_{\text{rca}} \leftarrow 0$;
$V_{\text{rca}} \leftarrow 0$ at every point;
while *dipoles continue to be identified* **do**
    for $i \leftarrow 1$ **to** n_v **do**
        if *vortex i is mutual nearest neighbours with some other vortex j* **then**
            if $V_p[i] \neq V_p[i]$ **then**
                $V_{\text{rca}}[i] \leftarrow -1$;
                $V_{\text{rca}}[j] \leftarrow -1$;
            end
        end
    end
end
while *vortices continue to be added to clusters* **do**
    for $i \leftarrow 1$ **to** n_v **do**
        for $j \leftarrow 1$ **to** n_v **do**
            if $V_{\text{rca}}[i] < 0$ **or** $V_{\text{rca}}[j] < 0$ **then continue**;
            if *vortex i and j are closer to one another than one of opposite polarity* **then**
                if $V_{\text{rca}}[i] > 0$ **and** $V_{\text{rca}}[j] = 0$ **then** $V_{\text{rca}}[j] \leftarrow V_{\text{rca}}[i]$;
                else if $V_{\text{rca}}[i] = 0$ **and** $V_{\text{rca}}[j] > 0$ **then** $V_{\text{rca}}[i] \leftarrow V_{\text{rca}}[j]$;
                else if $V_{\text{rca}}[i] > 0$ **and** $V_{\text{rca}}[j] > 0$ **then** (All $V_{\text{rca}} = V_{\text{rca}}[i]$) $\leftarrow V_{\text{rca}}[j]$;
                else
                    $n_{\text{rca}} \leftarrow n_{\text{rca}} + 1$;
                    $V_{\text{rca}}[i] \leftarrow n_{\text{rca}}$;
                    $V_{\text{rca}}[j] \leftarrow n_{\text{rca}}$;
                end
            end
        end
    end
end

Algorithm 6: The Recursive Cluster Algorithm. Decomposes a list of vortices into vortex dipoles or clusters. Vortices are labelled with a cluster number, with vortex dipoles labelled with -1.

3.3.2 Ripley's K function

$$K(x) = \frac{A}{n^2} \sum_{i \neq j} I\left(d_{ij} < x\right), \tag{3.2}$$

where d_{ij} is the distance between the ith and jth points, A is the area of the region containing every point, n is the number of points, x is the search radius, and I is the indicator function (1 if its argument is true, 0 otherwise). Should the points be distributed homogeneously in space, then $K(s) \approx \pi s^2$.

3.4 Tracking vortex trajectories

3.5 Removing vortices with phase unwrapping

input : A $n_x \times n_y$ complex field ψ. A 'safe' distance d. Vortex core radius c.
output: A $n_x \times n_y$ complex field ϕ.

```
φ ← ψ;
(n_v, V_l, V_p) ← Algorithm 5 ← ψ;
for i ← 1 to n_v do
    if |V_l[i]| > d then
        Imprint a vortex of polarity V_p[i] at location V_l[i] in φ;
        for j ← −c to c do
            for k ← −c to c do
                x ← V_l[1, i] + j;
                y ← V_l[2, i] + k;
                φ(x, y) ← ψ_inf × phase(ψ(x, y));
            end
        end
    end
end
```

Algorithm 7: The 'vortex killer' algorithm. By accurately imprinting a vortex, this algorithm removes vortices from the input wavefunction non destructively.

Part III

Numerical Studies

Chapter 4

Vortex deflection

4.1 Comparison of deflection from a vortex and an impurity

4.2 Special Cases

Chapter 5

Classical-like wakes behind elliptical obstacles in Bose-Einstein condensates

5.1 Introduction

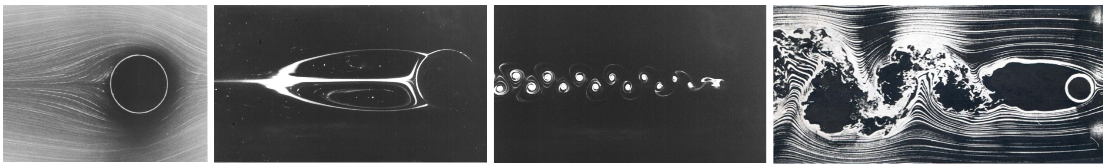

Figure 5.1: Classical viscous flow past a cylinder. From left to right: laminar flow ($Re = 3.64$) [3]; steady symmetric wake behind the cylinder ($Re = 41$) [3]; time-dependent Bénard–von Kármán vortex street ($Re = 112$) [4]; and chaotic downstream wake ($Re > 10^5$) [5].

Recent experimental [6, 7], numerical [8, 9, 10] and theoretical studies [11] have highlighted similarities between turbulence in quantum fluids (e.g. superfluid helium and atomic Bose-Einstein condensates) and turbulence in ordinary (classical) fluids [12]. In particular, it is found that, in the idealized case of homogeneous isotropic conditions away from boundaries, the distribution of kinetic energy over the length scales obeys the celebrated Kolmogorov scaling of classical turbulence [13]. This similarity is remarkable, because a superfluid has zero viscosity and vorticity is not a continuous field but is concentrated in discrete vortex filaments of fixed circulation κ proportional to Planck's constant. In the more realistic presence of boundaries (such as an obstacle or confining channel walls), superfluid hydrodynamics is less understood, despite the large number of experiments in such scenarios.

In a classical viscous fluid [12], the prototype problem with a boundary is the flow around a cylinder or a sphere (or, changing the frame of reference, the motion of a cylinder or a sphere in a fluid at rest). The nature of such flow is determined by the Reynolds number $Re = vd/\nu$, where v is the (assumed uniform) flow's velocity away from the obstacle, d is the obstacle's size, and ν is the fluid's kinematic viscosity. If $Re \lesssim 50$, a steady symmetric wake forms behind the obstacle; if $10^2 \lesssim Re \lesssim 10^5$ the wake becomes asymmetric and time dependent, forming the famous Bénard–von Kármán vortex street structure. These cases are depicted in Figure 5.1. At even higher *Re*, the flow becomes turbulent.

What happens in a superfluid is not clear. Firstly, the superfluid has zero viscosity ($\nu = 0$) and hence *Re* cannot be defined. Secondly, experiments performed in superfluid helium confirm that the flow is affected by the boundaries [14, 15]; unfortunately what is observed is not the flow pattern itself, but rather the trajectories of tracer particles, whose relation with the flow is still the subject of investigations [16]. Numerical simulations of three-dimensional (3D) superfluid flow around an oscillating sphere performed using the vortex filament model were not conclusive - quantum vortices did not appear to organise themselves into a visible classical–like wake near the obstacle [17, 18, 19].

The two-dimensional (2D) scenario of an obstacle moving through a superfluid offers a simplified platform to consolidate analogs and disparities between classical and quantum fluids. In their pioneering simulations of the 2D nonlinear Schrödinger equation, Frisch and Pomeau [20] observed the formation of vortex pairs in the flow past a circular obstacle. A more complete picture has been recently revealed by Sasaki *et al.* [21]. Below a critical velocity (which depends on the strength [22] and shape of the external potential), the fluid undergoes laminar flow around the obstacle. Above this critical velocity vortices become nucleated and peel off from the moving obstacle. Two patterns are possible, depending on the size of the obstacle: vortex-antivortex pairs in either a symmetric [20] or asymmetric configuration (with the preference for the latter); or alternating pairs of like-signed vortices, forming a trail analogous to the Bernárd-von Kármán vortex street. At higher velocities, vortex nucleation becomes highly irregular. Recent studies of this 2D system have considered vortex emission and drag [23, 24, 25, 26], the critical velocity [27, 28, 29, 30, 31], the effect of inhomogeneous potentials [25, 32, 33], the role on the obstacle parameters [26, 34], and supersonic effects such as oblique dark solitons [35] and Cerenkov radiation [36].

In this work we present the first clear evidence of a classical wake in superfluid flow past an obstacle. Using the Gross-Pitaevskii equation (GPE) for a zero-temperature Bose-Einstein condensate and an elliptical obstacle, we show that the interaction of discrete vortex singularities downstream of the obstacle yields a flow pattern which indeed mimics classical vortex flow.

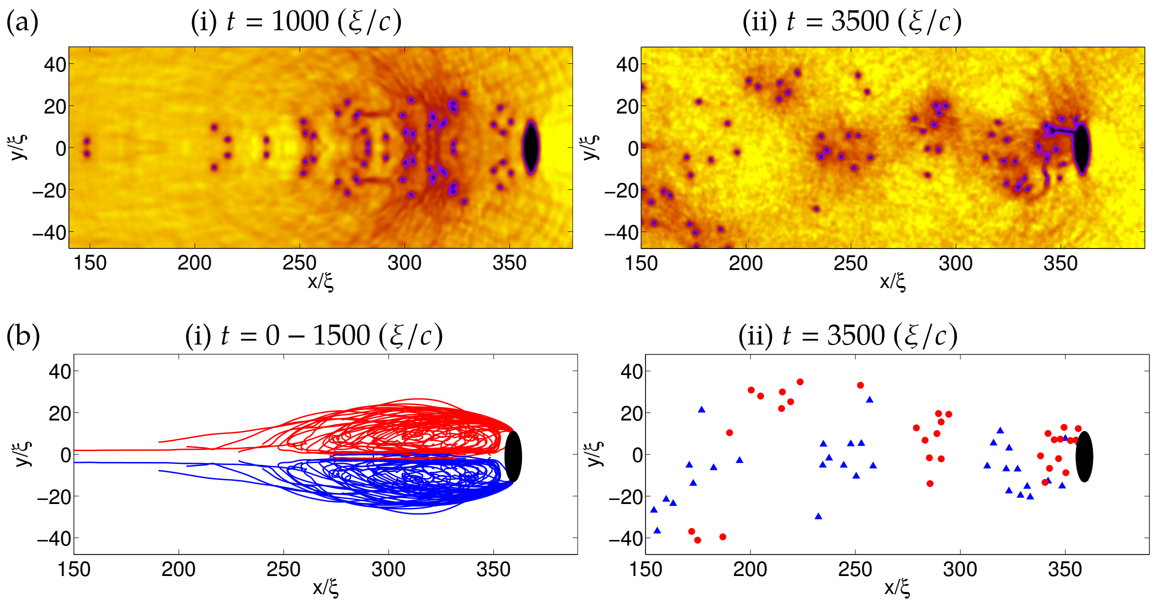

Figure 5.2: Snapshots showing the (a) density profile and (b) vortex trajectories during vortex shedding from an elliptical object ($\varepsilon = 3$) at (i) early times and (ii) later times. The obstacle has speed $v = 0.52c$ and size $d = 5\xi$. Red and blue lines represent vortices of oppositely quantized circulation. At early t, a symmetric wake similar to a classical fluid with low Re forms. Symmetry breaks at $t \approx 1500\ (\xi/c)$ at which point vortex motion becomes disordered. In this case the initial condition is noise-free.

5.2 Model

The external potential acting on the system $V(\mathbf{r}, t)$ is taken to be zero everywhere, i.e. a homogeneous system with uniform density n_0, apart from a localized repulsive potential, Gaussian in shape, which represents the obstacle. A key feature of this work is that the obstacle is taken to be elliptical, of ellipticity ϵ, with the short axis being parallel to the flow, x. Such a potential, in its 2D form, can be generated via the repulsive optical dipole force from an incident blue-detuned laser beam which is moved relative to the condensate either by deflection of the beam [37, 38, 39] or motion of the condensate itself when offset in a harmonic trap [40]. While laser-induced obstacles generated to date have had a circular profile, elliptical modification of the Gaussian potential can be achieved via cylindrical focussing of the laser beam.

We express length in terms of the healing length $\xi = \hbar/\sqrt{mn_0 g}$, speed in terms of the speed of sound $c = \sqrt{n_0 g/m}$, and time in terms of (ξ/c). A detailed description of the model can be found in Appendix A.

5.3 Results: Two-Dimensional Wakes

We begin by exploring quantum wakes in the 2D flow of a BEC past an obstacle, according to the 2D GPE with the elliptical potential defined in Equation (2.15).

5.3.1 Vortex emission from elliptical obstacles

For illustrative purposes we first consider an elliptical obstacle (size $d = 5\xi$, ellipticity $\epsilon = 3$) moving at speed $v = 0.365c$. This speed exceeds the critical velocity for the obstacle such that quantum vortices become nucleated and trail behind to form a wake [Figure 5.2(a)]. Sound waves, also generated by the obstacle, have little effect on the vortex dynamics. At early times [Figure 5.2(a)(i)], the vortex shedding occurs through the symmetric generation of vortex-antivortex pairs, leading to a collimated and symmetric wake behind the obstacle. This is in qualitative agreement with observations for circular obstacles [20, 23, 25, 26], although, for the same obstacle velocity and size, the elliptical obstacle induces a higher frequency of vortex emission and thus a denser wake. We examine the role of ellipticity in more detail in Sections 5.3.3 and 5.3.4.

At later times [Figure 5.2(a)(ii)], the flow becomes asymmetric due to the known instability of symmetric wakes [23]. A striking pattern emerges whereby distinct clusters of co-rotating vortices (of the order of 5 vortices in each cluster) develop downstream of the obstacle. Each cluster contains vortices of the same sign and adjacent clusters have alternating sign. These clusters form a Bénard–von Kármán vortex street downstream from the obstacle, confirming the intuition that a sufficiently large number of quanta of circulation reproduce classical physics. Here, the ellipticity of the obstacle facilitates the formation of this street; the relatively high rate of vortex emission leads to a greater interaction between vortices in the wake which in turn promotes clustering. In contrast, for a circular obstacle the symmetric wake evolves into a V-shaped wake of vortex-antivortex pairs [21]; this because the vortex emisson rate and hence their subsequent interaction is insufficient to induce significant clustering.

The vortex trajectories provide visualisation of the time-integrated nature of the wake [Figure 5.2(b)]. At early times (i), we see that the vortex trajectories are symmetric, forming a flow pattern in striking analog to the classical wake at low Re. The generic development of vortex trajectories is as follows. Pairs of singly-quantized vortices of opposite sign peel off from the poles of the obstacle and interact with each other as vortex-antivortex pairs. Each pair propagates in the positive x direction with approximate velocity $\hbar/(md_p)$[21], where d_p is the pair separation [41]; the pair's velocity is less than the obstacle's velocity and it drifts behind the obstacle. As the pair moves further away from the obstacle, its separation decreases and its velocity increases, such that it begins to catch the obstacle up. Once the pair is sufficiently close to the obstacle, it again separates and slows down, then

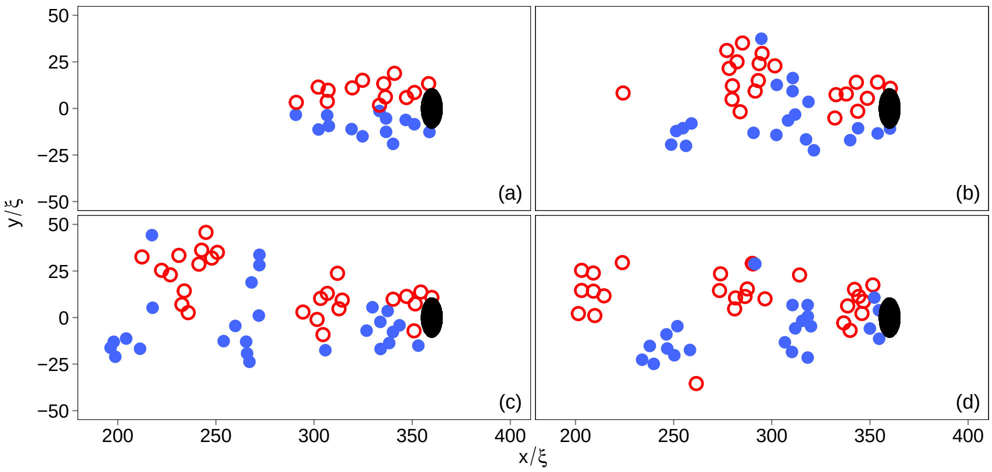

Figure 5.3: Snapshots of vortex locations during the motion of an elliptical object ($d = 5\xi$ and $\varepsilon = 3$) at speed $v = 0.52c$ in the presence of small-amplitude noise at $t = 0$. The snapshots are at times (a) $t = 450$, (b) 900, (c) 1000 and (d) 1100 (ξ/c). Red/blue circles represent vortices with quanta of circulation $+1/-1$. The wake forms into clusters of like-circulation that continue to be produced, in analogy to the classical Bénard–von Kármán vortex street from a cylinder.

the cycle repeats. As more vortices are nucleated, two distinct clusters of like-circulation form. Nucleated pairs then travel around the outside of the existing cluster before contracting, speeding up and travelling through the middle of the clusters towards the obstacle. The clusters grow until they reach a maximum size depending on the obstacle's size and speed. Hereafter, nucleated vortex pairs travel around the outside of the two clusters and continue travelling downstream, becoming lost from the main wake.

5.3.2 Formation of the Bénard–von Kármán vortex street

Once the symmetry of the wake is broken, vortices no longer separate into two distinct clusters of like-circulation. Existing vortices and newly-nucleated vortices mix together behind the obstacle. However it is apparent in Figure 5.2(b)(ii) that, on average, positive vortices drift to $y > 0$ while negative vortices prefer to drift to $y < 0$.

To accelerate the formation of the asymmetric wake, we subsequently seed the initial condition with noise. Figure 5.3 shows the vortex locations at various stages of the evolution. The initial symmetry of the wake [Figure 5.3(a)] breaks at $t \approx 450(\xi/c)$, with the wake splitting into several clusters. The velocity field around the obstacle is affected: it depends on time and the distance of the nearest cluster of vortices. The obstacle no longer simultaneously produces vortex-antivortex pairs, but now generates a series of like-signed vortices. Since like-signed vortices are known to co-rotate, these vortices group into clusters which slowly rotate. This cluster effects the velocity field once more, causing a cluster of opposite signed vortices to be produced. This process then repeats such that clusters

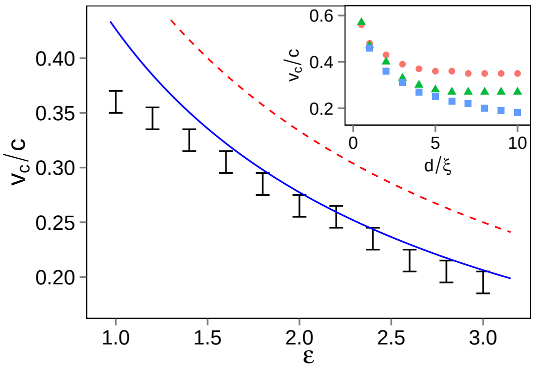

Figure 5.4: Critical velocity against obstacle ellipticity ε, for $d = 10\xi$. Shown are the results from the numerical simulations (black bars), Equation (5.1) (dashed red line) and Equation (5.2) (solid blue line). Inset: Critical velocity (obtained numerically) versus the obstacle width d, for ellipticities $\varepsilon = 1$ (red circles), $\varepsilon = 2$ (green triangles) and $\varepsilon = 3$ (blue squares).

of like signed vortices are then produced behind the obstacle, much like vorticity in the classical vortex street behind a cylinder. While some positive clusters contain negative vortices and vice versa, the overall pattern is still a time-dependent Bénard–von Kármán vortex street.

For clusters consisting of pairs of vortices, it has been shown that they can survive downstream for a very long time [21]. However, for regimes with larger numbers of vortices in each cluster, the chaotic nature of vortex motion can cause originally tightly packed and circular clusters to easily stretch over large areas, form strange shapes, or even split into smaller clusters. Examples of this will be shown later in Figure 5.5.

5.3.3 Critical Velocity past an Elliptical Obstacle

Elliptical obstacles facilitate the formation of semi-classical wakes because they reduce the critical velocity and enhance the vortex shedding frequency. Figure 5.4(a) shows the critical velocity for flow past the obstacle as a function of its ellipticity, taking the obstacle to have fixed width in the y-direction of $d = 10\xi$. We determine the critical velocity numerically by performing simulations with flow velocities increasing in steps of 0.01 until vortices nucleate. For a circular object, we find that the critical velocity is $v_c = 0.355(\pm 0.005)c$, consistent with predictions in the Eulerian ($d \gg \xi$) limit [29, 30, 31]. As the ellipticity is increased (i.e. the obstacle becomes narrower in x), the critical velocity decreases. The modification of the critical velocity is significant: if $\varepsilon = 3$, v_c is more than 40% smaller than that for a circular obstacle.

The rough dependence of v_c on ε can be derived as follows. According to Landau's criterion [42], superfluidity breaks down when the fluid velocity exceeds the critical velocity $v_{\mathrm{Lan}} = \min\left[E(p)/p\right]$, where p is the momentum of elementary excitations and

$E(p)$ their energy. The weakly-interacting Bose gas has the dispersion relation $E(p) = [ngp^2/m + p^4/(4m^2)]^{1/2}$, hence $v_{\text{Lan}} = c$. If an obstacle moves through the fluid with speed v, the local fluid velocity at the poles exceeds v. Approximating the BEC as an inviscid Euler fluid undergoing potential flow about the object, then the maximum local velocity is $v_{\max} = (1+\varepsilon)v$ and the Landau critical velocity is (dashed red line in Figure 5.4(a)),

$$\frac{v_{c1}}{c} = \frac{1}{1+\varepsilon}. \tag{5.1}$$

While this result assumes constant density, a first order correction can be made by using Bernoulli's theorem to model the reduction in local density near the obstacle (due to the enhanced local fluid velocity) which in turn reduces the local speed of sound $c(x, y) = \sqrt{n(x, y)g/m}$ [43]. This then leads to the modified result,

$$\frac{v_{c2}}{c} = \left[\frac{3}{2}(1+\varepsilon)^2 - \frac{1}{2}\right]^{-\frac{1}{2}}. \tag{5.2}$$

This relation (solid blue line in Figure 5.4) gives good agreement with the computed values of v_c. The deviation for $\varepsilon \sim 1$ has been noted elsewhere [30], and can be remedied using higher order corrections.

From studies on circular objects, it is known that v_c depends on the obstacle's shape at small diameters, where boundary layer effects are significant; v_c approaches the "Eulerian" value only for large diameters $d \gg \xi$ [26, 30]. The variation of v_c with the obstacle width d is shown in Figure 5.4 (inset). For $d = 10\xi$, the critical velocity effectively reaches its asymptotic value, while at smaller widths, it is much larger.

5.3.4 Role of Obstacle Size and Ellipticity on the Wake

During the initial symmetric phase of vortex nucleation, the wakes generated by the obstacle have the same qualitative structure shown in Figure 5.2(b) (i). However, once the wake becomes asymmetric, the nature of the clusters that form are highly dependent on the velocity and shape of the obstacle. Figure 5.5 shows wakes generated for various obstacle parameters, all captured at the same time $t = 2000$ (ξ/c). We find that any increase of size, ellipticity or velocity of the obstacle increases the number of vortices in the wake's clusters.

The shedding frequency of vortices increases with the velocity of the flow [24]. For an elliptical obstacle, the combination of a reduced critical velocity and increased local velocity around the obstacle has the effect of increasing the shedding frequency with ε and d. The overall result is that, when increasing any of v, ε or d, more vortices are nucleated in a given time period, causing the cluster size to increase. This increase in cluster size is investigated in the next section.

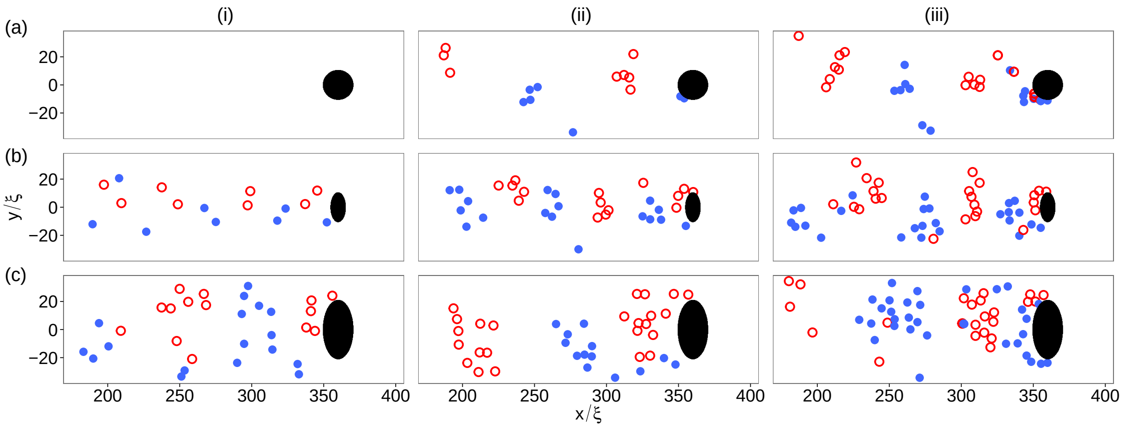

Figure 5.5: Snapshots of the vortex positions for various obstacle parameters, at $t = 2000$ (ξ/c). Shown are obstacles corresponding to (a) $\varepsilon = 1$ and $d = 5\xi$, (b) $\varepsilon = 2$ and $d = 5\xi$, and (c) $\varepsilon = 2$ and $d = 10\xi$, at the velocities (i) $v = 0.32c$, (ii) $v = 0.40c$, and (iii) $v = 0.48c$. Red/blue circles represent vortices with quanta of circulation $+1/-1$.

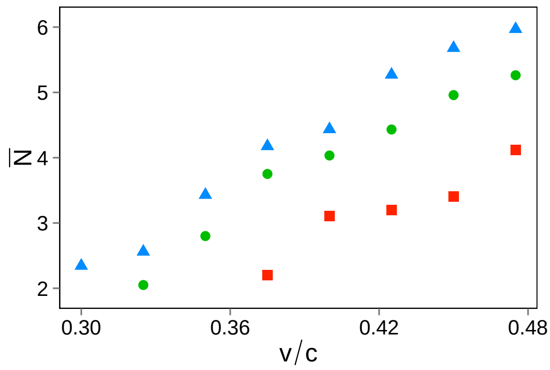

Figure 5.6: Average number of vortices in the clusters as a function of the obstacle velocity v. Shown are cases with $\varepsilon = 1$ (red squares), $\varepsilon = 2$ (green circles) and $\varepsilon = 3$ (blue triangles). All cases feature $d = 5\xi$.

5.3.5 Vortex Clustering

We have shown that the Bénard–von Kármán vortex street forms through the clustering of like-signed vortices. Methods of quantifying the clustering of vortices in quantum fluids have been explored in the literature [44, 45, 46]. Here we utilize the algorithm of Reeves *et. al.* [45] to identify clusters.

Firstly we record the number of clusters N_c and the number of vortices in each cluster N_i, where i is the cluster index. Then we determine the average number of vortices in the clusters, $\bar{N} = (1/N_c)\sum_{i=1}^{i=N_c} N_i$ as a function of obstacle velocity v for three ellipticities $\varepsilon = 1, 2$ and 3, at times $t = 500(\xi/c), 510(\xi/c), \ldots, 2500(\xi/c)$. The results, plotted in Figure 5.6, show that increasing v (above the critical velocity) causes $\bar{N}$ to increase and that, at fixed v, $\bar{N}$ increases with ε. We attribute this to an object with a larger ε having a lower

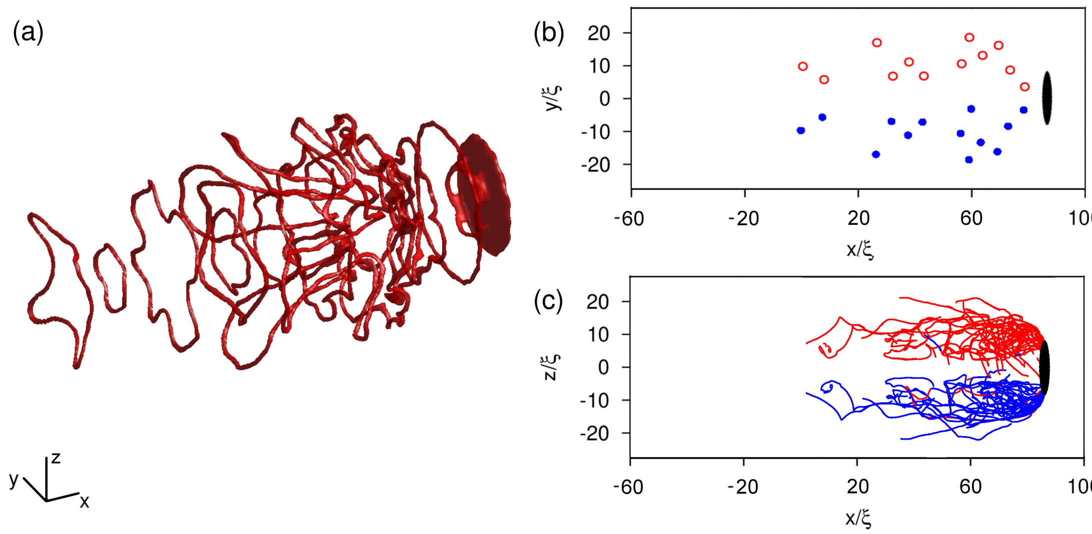

Figure 5.7: Symmetric wake in 3D at $t = 450$ (ξ/c) for an elliptical obstacle ($d = 5\xi$ and $\epsilon = 5$) moving at $v = 0.6c$. (a) Isosurface plot of low density, over a range $[0, 100]$ in x and $[-25, 25]$ in y and z. (b) Vortex locations in the xy plane. (c) Vortex trajectories in the xz plane. Here (b) and (c) show opposing circulation in red and blue.

critical velocity and producing more vortices at the same v. This result explains why an elliptical obstacle efficiently generates a semi-classical wake composed of large vortex clusters. We also find that for all values of ε, a large obstacle velocity ($v \gtrsim 0.6$) causes vortices to nucleate non-periodically, inducing an irregular flow without a visible Bénard–von Kármán vortex street configuration, in agreement with previous simulations with circular obstacles of smaller diameter [21].

5.4 Results: Three-Dimensional Wakes

We now generalize our results to 3D by considering quantum wakes in three-dimensional flow past a localized obstacle, as simulated via the 3D GPE with the 3D obstacle potential of Equation (2.14). Our results will confirm that the features observed in 2D wakes also arise in the 3D setting. A comprehensive study of the parameter space is, however, not tractable in 3D due to the computational intensity of the 3D simulations.

5.4.1 Symmetric Wakes

For a spherical ($\varepsilon = 1$) object with $d = 5\xi$, we find that the critical velocity is $v_c = 0.455 \pm 0.05c$, consistent with $v_c = 0.55c$ reported in the Eulerian limit ($d \gg \xi$) [43, 47]. Making the obstacle ellipsoidal, with the short direction parallel to the flow, reduces the critical velocity, in parallel with our 2D observations. For example, for $\varepsilon = 5$, the critical velocity is reduced to $v_c = 0.315 \pm 0.05c$. Figure 5.7(a) shows the 3D wake generated past this

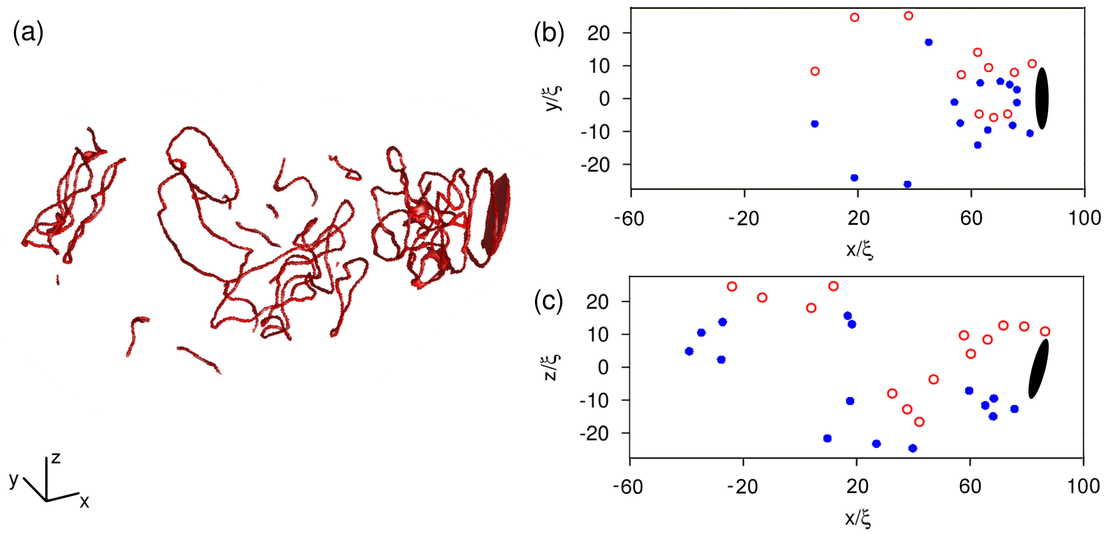

Figure 5.8: Asymmetric wake in 3D at $t = 340\ (\xi/c)$ for an elliptical obstacle ($d = 5\xi$ and $\epsilon = 5$) moving at $v = 0.6c$. (a) Isosurface plot of low density, over a range $[-60, 100]$ in x and $[-25, 25]$ in y and z. (b) Vortex locations in the xy plane. (c) Vortex locations in the xz plane. Here (b) and (c) show opposing circulation in red and blue.

ellipsoidal obstacle ($d = 5\xi$ and $\varepsilon = 5$) when moving at super-critical speed $v = 0.6c$. Vortex rings, the 3D analog of vortex-antivortex pairs, are ejected at high frequency (due to the obstacles high ellipticity) in the direction of the flow. At early times ($t = 450\ (\xi/c)$ in this case) the vortex configuration maintains cylindrical symmetry about the obstacle's axis, as is clearly visible in the xy and xz planes in Figure 5.7(b) and (c). As the vortex rings move downstream they shrink and speed up, returning to the object, sometimes passing through other vortex rings. A similar behaviour is observed [48] in the evolution of toroidal bundles of many coaxial vortex rings which leapfrog around each other. Occasionally a ring will escape this cycle and fall downstream. These behaviors conspire to form an organized symmetric wake behind the obstacle, the 3D analog of our 2D observations.

5.4.2 Asymmetric Wakes

We break the cylindrical symmetry of the system by tilting the obstacle by a small angle in the xz plane. The vortex rings, illustrated in Figure 5.8, now become ejected and evolve asymmetrically; Kelvin waves and reconnections occur, forming an apparently disordered tangle of vortices behind the obstacle. Due to the manner in which symmetry is broken, the wake remains approximately symmetric in the xy plane, as evident in Figure 5.8 (b). However, unlike in Figure 5.8, the vortices do not self organise into two clusters of alternate circulation. This is due to the vortex rings interacting, reconnecting and shifting out of the plane (which manifests in 2D as two alternate-sign vortices approaching one another).

However, in the xz plane (Figure 5.8 (c)), symmetry is broken. Due to the relatively high frequency of vortex nucleation and relatively low flow speed, like signed vortices cluster together as they are ejected by the obstacle, much like the 2D solutions seen in earlier sections. Downstream the tangle may shift both across or out of the plane. In 2D, although this manifests as a shift in location of the vortex clusters, the clusters largely remain rather than forming dipoles.

5.5 Conclusion

We have shown that the motion of an obstacle in a Bose-Einstein condensate produces classical-like wakes consisting of quantum vortices of the same polarity. This is consistently observed in both two- and three-dimensional scenarios. The key ingredient to produce classical-like wakes - that vortices are generated at a sufficiently high rate that they undergo strong interactions with their neighbours (rather than being swept away) - is that the obstacle is elliptical, which reduces the critical velocity for vortex nucleation. Symmetric wakes resemble those observed in classical flow at low *Re*. These are unstable, forming time-dependent asymmetric structures similar to the Bénard–von Kármán vortex street of classical fluid dynamics. Vortex singularities in the inviscid superfluid thus mimic classical vortex patterns typical of viscous flows. The effects which we describe (dependence of the critical velocity and cluster size on the obstacle's size, velocity and ellipticity) can be experimentally studied in atomic Bose-Einstein condensates using moving laser-induced potentials. They are also relevant to the motion of objects (such as vibrating wires, grids and forks) in superfluid helium, as the obstacle's ellipticity plays a role which is analogous to rough boundaries [49, 50].

5.6 Model of 2D and 3D BEC with Gaussian Potentials

The 3D (2D) system is simulated using the 4th-order Runge-Kutta method under periodic boundary conditions on a $400 \times 150 \times 150$ (2048×512) grid with uniform spacing $\Delta = 0.4\xi$. The obstacle is positioned upstream in the box to enable a long simulation time before vortices recycle through the periodic box. We have verified that our simulations are well-converged, that is, increasing the grid resolution has negligible effect on the results. The computational box is sufficiently large that the boundary conditions do not play a role in vortex shedding. The initial condition is the stationary state of the GPE (including obstacle potential) with $v = 0$ (as determined by the imaginary time convergence method). Setting $V_0 = 100\,\mu$ throughout, the external potential closely approximates an impenetrable obstacle. Unless stated otherwise, a small amount of noise is added to the initial condition to break symmetry: a random number between -0.0005 and 0.0005 is added to both the real and imaginary parts of the initial wavefunction.

To minimize initial generation of waves, v is ramped up in time along a hyperbolic tangent curve, from $v = 0$ at $t = 0$ to its terminal value at around $t \approx 100\ (\xi/c)$. During the evolution, the vortices are located (and their circulation evaluated) using an algorithm based on those of references [51] and [44].

Chapter 6

Decay of 2D quantum turbulence in a highly oblate Bose-Einstein condensate

6.1 Introduction

Ultracold gaseous Bose-Einstein condensates (BECs) provide a unique testbed with which to investigate the phenomenon of quantum turbulence and the more rudimentary realm of superfluid vortex dynamics [52, 53]. These systems provide an impressive degree of parameter manipulation unavailable in superfluid helium, the traditional context for studying quantum turbulence [54], with scope to control the particle interactions and potential landscape in both time and space. The typical size of these systems is only one or two orders of magnitude larger than the inter-vortex spacing, which in turn is another order of magnitude larger than the vortex core size. These compact length scales mean that the collective behaviour of vortices and their interaction with the background condensate is significant. The emergence of turbulent-like behaviour in the form of a vortex tangle was observed by Henn *et al.* in 2009 by oscillating a three-dimensional condensate [55]. What's more, the experimentalist's handle over the confining potential enables crossover to two-dimensional quantum turbulence [56]: by tightly confining the trap geometry along one axis, such that the vortices closely embody point vortices [57], states of two-dimensional quantum turbulence have been recently reported [58, 59].

In the recent experiment of Kwon *et al.* [59], a trapped, oblate BEC was translated past a stationary, laser-induced obstacle. As is characteristic of superfluids, vortices and anti-vortices were nucleated into the condensate once the relative speed exceeded a critical value [20]. A state of two-dimensional quantum turbulence emerged, characterized by a disordered distribution of vortices. The authors monitored the number of vortices, revealing the dependence on the relative speed and the thermal relaxation of the vortices. They directly observed vortex collision events, characterized by a crescent-shaped depletion in the condensate density. Furthermore, some vortex cores were seen to coalesce, evidence of vortex pair annihilation.

In this article we elucidate these experimental findings through mean-field simulations of the two–dimensional (2D) Gross-Pitaevskii equation (GPE), both at zero-temperature and in the presence of thermal dissipation, modelled through a phenomenological dissipation term in the GPE. Notably, our simulations provide insight into the sign of the circulation of the vortices and the early-stage evolution, not accessible experimentally. We establish the key stages of the dynamics, from the initial nucleation of vortices and formation of a quasi-classical wake, through the rapid symmetry breaking and disorganization of the vortices, to the decay of the vortices by annihilation or passage out of the condensate. Our approach gives excellent agreement with the experimental observations.

6.2 Set-Up

In the experiment, a ^{23}Na condensate with $N = 1.8 \times 10^6$ atoms was confined within a highly-oblate cylindrically symmetric harmonic trap $V_{\text{trap}}(x,y,z) = \frac{1}{2}m[\omega_r^2(x^2+y^2)+\omega_z^2 z^2]$, with axial frequency $\omega_z = 2\pi\times350$ Hz and radial frequency $\omega_r = 2\pi\times15$ Hz (corresponding to an aspect ratio parameter $\omega_z/\omega_r \approx 23$) and where m denotes the atomic mass. A 2D mean-field description is strictly valid when the condition $Nal_z^3/l_r^3 \ll 1$ is satisfied, where $l_z = \sqrt{\hbar/m\omega_z}$ and $l_r = \sqrt{\hbar/m\omega_r}$ are the axial and radial harmonic oscillator lengths and a is the s-wave scattering length [60, 61]. For this experiment, $Nal_z^3/l_r^3 = 8.3$, i.e. the system remains 3D in nature. Nonetheless, the dynamics of the vortices is essentially 2D because of the suppression of Kelvin waves in the z-direction [62]. Therefore, we will adopt a 2D description throughout this work and show that it is sufficient to capture the experimental observations. It is worth noting that in the xy plane the condensate closely approximates a Thomas-Fermi (inverted parabola) density profile with radius $R_{\text{TF}} \approx 70\mu m$.

We parameterize the condensate by a 2D wavefunction $\phi(x,y,t)$; the condensate density distribution follows as $n(x,y,t) = |\phi(x,y,t)|^2$. The wavefunction satisfies the 2D GPE:

$$i\hbar\frac{\partial\phi}{\partial t} = \left(-\frac{\hbar^2}{2m}\nabla^2 + V(x,y,t) + g|\phi|^2 - \mu\right)\phi \tag{6.1}$$

where μ denotes the chemical potential of the condensate and $g = 2\hbar a(2\pi\omega_z\hbar/m)^{1/2}$ characterizes the effective 2D nonlinear interactions arising from s-wave atomic collisions. We solve the GPE on a 1024×1024 grid using a fourth-order Runge-Kutta method. The vortex core size is characterized by the healing length $\xi = \hbar/\sqrt{mng}$; at the condensate centre this has the value $\xi \approx 0.6\mu$m. The grid spacing is $0.27\mu m$ in both x and y, and we have verified that reducing the grid spacing has no effect on our results.

Following the experiment, the total potential acting on the condensate $V(x, y, t)$ is the above harmonic trap plus a static Gaussian-shaped obstacle potential $V_{\rm obs}(x, y) = V_0 \exp[-2(x^2 + y^2)/d^2]$, located at the origin, with $V_0 = 15\mu$ and $d = 15\mu$m. The initial ground-state BEC is obtained by solving the GPE in imaginary time with enforced norm $N = 1.8 \times 10^6$. At $t = 0$ the harmonic trap is centered at $x = 18.5\mu$m. The trap is translated towards the left, at speed v, over a distance of 37μm; to smooth this speed curve we additionally include a linear acceleration/deceleration over 3.75ms at the start/end, which is included as part of the 37μm translation. Once the trap is at rest, the obstacle amplitude V_0 is ramped down to zero over 0.4s.

6.3 Results

6.3.1 Number of Vortices Generated

Following removal of the obstacle, we determine the number of vortices in the system N_v (performed by identifying locations where the condensate possesses a 2π singularity in the phase). We limit our search to 75 percent of the Thomas-Fermi radius (centred on the centre-of-mass to account for sloshing motion); by avoiding the low density periphery we avoid artifacts from ghost vortices and match closely what is performed experimentally (since vortices close to the edge are not detected due to low signal-to-noise [63]). In Fig. 6.1 we plot N_v versus the translation speed v. We see the same *qualitative* form between our simulations (red circles) and the experiment (black crosses): above a critical speed $v_c \approx 0.45$mm/s vortices enter the system, nucleated by the relative motion between the obstacle and the superfluid, and for $v > v_c$ the growth in N_v is initially rapid but tails off for $v \gg v_c$. Quantitatively, however, the GPE overestimates N_v. One can expect that thermal dissipation, not accounted for in the GPE, will act to reduce the number of vortices in the system. We introduce the effects of such dissipation via the addition of phenomenological dissipation, γ [64, 65], which enters the GPE (6.1) by replacing i on the left hand side by $(i - \gamma)$. This term induces the decay of excitations; for single vortices this manifests in them spiraling out of the trapped condensate [66, 62, 67, 68]. We choose a small value $\gamma = 0.0003$ so as to model the experiment in its very coldest realization of ~ 130nK and enforce the norm throughout the dissipative simulations so as to emulate the experiment (for which no significant loss of atom number was observed).

With this dissipation the data for N_v becomes reduced, bringing it closely in line with the experimental data. Experimental limitations in resolving and counting vortices may also contribute to the over-estimate of N_v from the GPE.

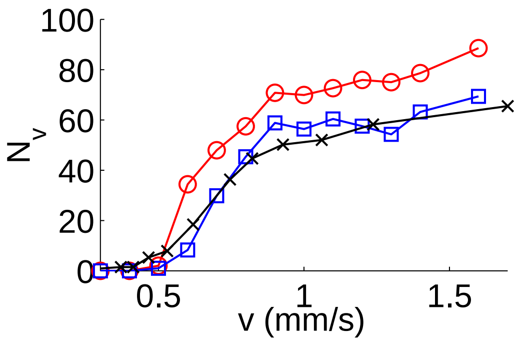

Figure 6.1: (Color online) Number of vortices N_v in the condensate after removal of the obstacle. Shown are simulations of the GPE without dissipation (red circles), with dissipation $\gamma = 0.0003$ (blue squares) and experimental results extracted from Fig. 1 of [59] (black crosses). Each point is averaged over 20 ms once the obstacle amplitude reaches $V_0 = 0$. For comparison, the speed of sound in the center of the BEC is $v_c \approx 4.6$ mm/s.

6.3.2 Stages of the Condensate Evolution

We now examine in detail the evolution of the condensate, charting its dynamics from the initial stage (when the harmonic trap translation begins) to the intermediate and final stages (randomization and decay of the vortices). We see the same qualitative evolution with and without dissipation, and for all velocities exceeding v_c. For the purposes of illustration, we focus on an example with dissipation and a translation speed $v = 1.4$mm/s.

Figure 6.2 shows the condensate density at various times. At the start of the simulation ($t = 0$) the condensate has a smooth circular density profile, with a density depression due to the obstacle. Later vortices appear as small dots of low density; superimposed red/blue markers tag vortices of positive/negative circulation.

Vortex Nucleation and Wake Formation

To initiate the dynamics, the harmonic trap is translated to the left. This is performed sufficiently rapidly that the condensate does not adiabatically follow the trap minimum, but rather begins a sloshing motion in the trap; the centre-of-mass of the BEC oscillates at the trap frequency and the BEC undergoes a quadrupolar shape oscillation. As the BEC sloshes first to the left, its speed increases. When the local fluid velocity exceeds the speed of sound [20], vortices nucleate at the poles of the obstacle (where the local fluid velocity is the greatest) and are washed downstream (to the left). The pattern of vortices nucleated by a moving obstacle in a superfluid depends, in general, on the speed, shape and size of the obstacle [22, 21, 69]. During the initial evolution vortices of negative and positive circulation are created near each pole in an irregular manner, sometimes with alternating circulation; other times several vortices of the same circulation appear. In our case, the rate of vortex nucleation is sufficiently high that the vortices interact strongly with each other, collectively forming macroscopic clusters of negative and positive vortices downstream of the object ($t = 43$ms). This is reminiscent of the wakes in classical viscous fluids past cylindrical obstacles [69]. During this early stage, vortices of opposite circulation may become very close and annihilate (i.e. undergo a 2D reconnection), leaving behind density

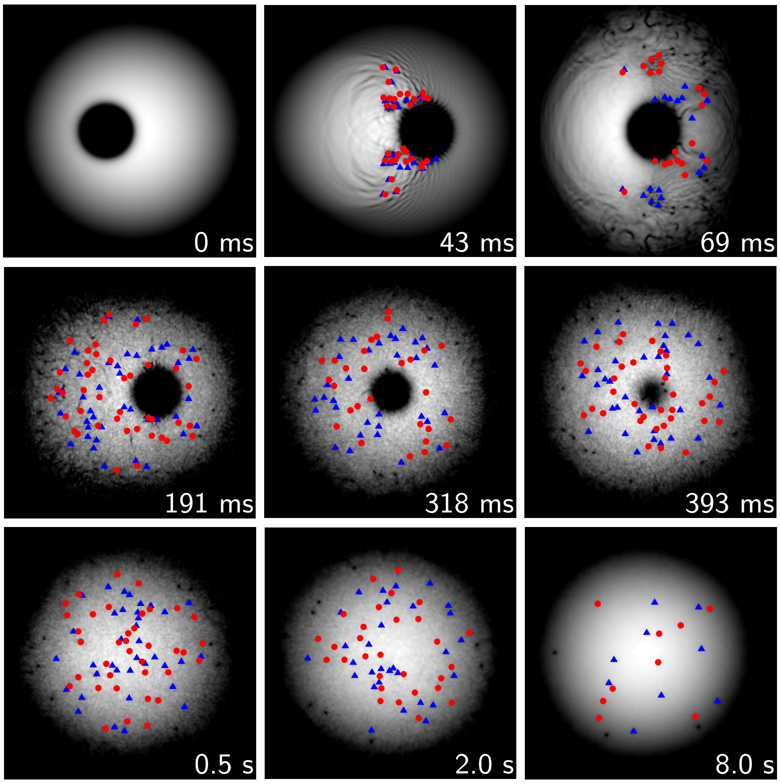

Figure 6.2: (Color online) Snapshots of the condensate density, for a translational speed v = 1.4mm/s and in the presence of dissipation ($\gamma = 0.0003$). The obstacle is completely removed at 0.43s. The field of view in each subfigure is of size $[170\mu\mathrm{m}]^2$ and shifted along the x-axis so as to best display the condensate. Vortices with positive (negative) circulation are highlighted by red circles (blue triangles).

(sound) waves. The condensate then sloshes to the right; this motion not only carries the existing vortices to the opposite (right) side of the obstacle but nucleates further vortices. As the condensate's sloshing mode is damped by the dissipation, the relative speed of the obstacle decreases and the vortex nucleation pattern changes: like-signed vortices are generated near each pole, forming symmetric classical–like wakes [69]. This effect leads to further clustering of like-signed vortices (t = 69ms). As the condensate continues to slosh, more vortices nucleate into the system. It must be stressed that, up to these early times (t = 191ms), the vortex distribution remains symmetric about the x axis. Without the dissipation term in the GPE, the sloshing mode initially decays while the obstacle is present but then persists with constant amplitude once the obstacle is removed. If dissipation is included then the sloshing mode continues to decay.

Figure 6.3: Growth of vortex number (in a single realization) at early times for a translational speed of $v = 1.4$mm/s. Shown are the results with no dissipation (red dashed line) and with dissipation $\gamma = 0.0003$ (blue solid line).

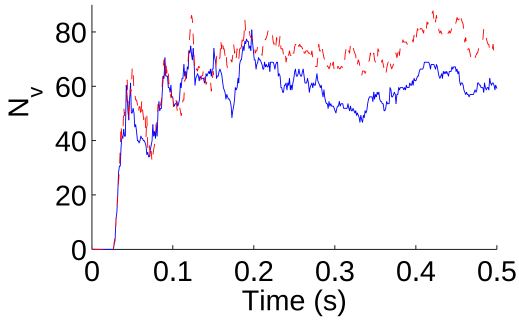

Vortex Randomization

In the presence of the obstacle and the sloshing mode, vortices continually nucleate and their spatial distribution remains approximately symmetric about the x axis. At later times ($t > 318$ms) this symmetry breaks and the vortices evolve into a completely disorganised, apparently random configuration with no significant clustering of like-signed vortices. This random distribution of vortices is consistent with the experimental observations [59]; following this we also classify the system as one of quantum turbulence. Besides vortices, the condensate contains also collective modes and an energetic, disordered sound field, with this spatial range of excitations further indicative of two-dimensional quantum turbulence [56, 58]. (Note that the typical characteristic diagnostics of steady-state 2D quantum turbulence, e.g. power-law energy spectra and the inverse energy cascade, are not appropriate here since the system is not continuously driven and does not reach steady state.)

The vortex randomization is driven by the growth of numerical noise. We have repeated our results in the presence of imposed noise (amplitude 5%, as described elsewhere [69]) and find the qualitative dynamics to be unchanged (although, as one would expect, the vortex randomization occurs at a slightly earlier time). This noise serves to model the natural fluctuations that arises in a realistic experimental scenario, e.g. due to thermal and quantum atomic fluctuations, electromagnetic noise, vibrations, etc.

It is interesting to note the obstacle is still in the system at this point, nucleating vortices in a symmetrical manner. The disorganised vortices already in the system create a velocity field which quickly mixes newly created vortices nucleated at the poles of the obstacle. Visual inspection, confirmed by a clustering-detection algorithm [44, 45], shows no significant clusters beyond this stage of the evolution. By the time the obstacle is removed the vortex configuration is essentially random, but the number of positive and negative vortices stays approximately equal. It is important to remark that, without detecting the sign of the vortex circulation, we could not reach these conclusions.

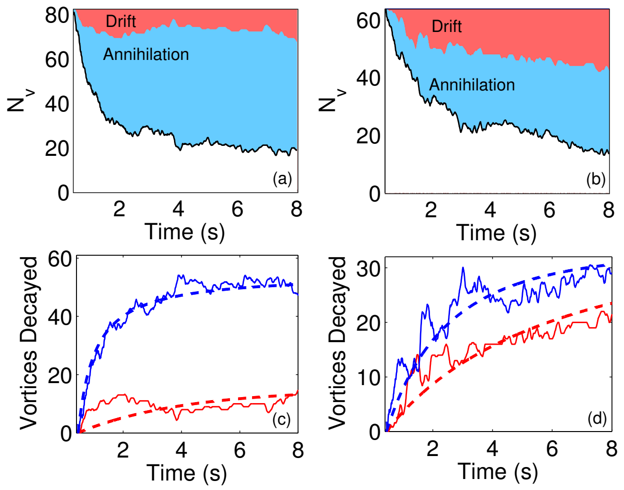

Figure 6.4: Vortex decay in the absence of dissipation (a, c) and with dissipation $\gamma = 0.0003$ (b, d) for a translational speed of $v = 1.4$mm/s. The upper figures show the decay of the total vortex number $N_v(t)$, with the contribution of drifting and annihilation depicted by the shaded regions. The lower figures show the drift number $N_d(t)$ and annihilation number $N_a(t)$, plus their respective fits.

Vortex Decay

It is clear from Fig. 6.2 that, following the removal of the obstacle, the number of vortices (N_v) depletes. Indeed, one expects that the condensate will decay towards its vortex–free, time–independent ground state. To quantify the vortex generation and decay, Fig. 6.3 plots N_v versus time. The onset of vortex nucleation is at around $t = 0.02$ms; this is the time taken for accelerating condensate to exceed the speed of sound at the poles of the object. At first N_v grows steeply, as vortices (around 40-60) are rapidly driven into the system. Subsequently, N_v grows more slowly; vortices continue to be nucleated from the obstacle but vortices undergo annihilation or move into low density regions where they are not detected. The fluctuations in N_v are amplified, particularly at early times, by the shape oscillations of the condensate, which carry vortices in and out of the detection radius. As the obstacle is removed at $t \approx 0.4$s, the surrounding condensate fills the low density area. Vortices (including some outside of the detection radius) move inwards with the flow, causing N_v to peak.

Following removal of the obstacle, the vortex number N_v decays with time. This is shown in Fig. 6.4(a) and (b) for the absence and presence of dissipation, respectively. Kwon *et al.* [59] argued that there are two mechanisms by which vortices decay: (i) thermal dissipation (resulting in drifting of vortices to the edge of the condensate), and (ii) vortex-antivortex annihilation events, and proposed that the vortex decay takes the form:

$$\frac{\mathrm{d}N_v}{\mathrm{d}t} = -\Gamma_1 N_v - \Gamma_2 N_v^2. \tag{6.2}$$

Here the linear and nonlinear terms, parameterized by the positive coefficients Γ_1 and Γ_2, respectively, model these two decay processes. From our simulations we are able to independently count the number of vortices which drift out and the number which annihilate. We decompose the number of vortices according to $N_v(t) = N_{v0} - N_d(t) - N_a(t)$, where N_{v0} is the initial number of vortices (when the obstacle is removed), $N_d(t)$ is the cumulative number of vortices which have drifted out of the condensate and $N_a(t)$ is the cumulative number which have undergone pair annihilation. The contribution of both vortex drifting and annihilation to the overall decay of N_v is depicted by the coloured regions in Fig. 6.4(a) and (b). In the absence of dissipation the vortex decay is dominated by annihilation. Indeed, apart from at early times (where internal condensate dynamics carry vortices out to high radii), no vortices drift out. In contrast, in the presence of dissipation, vortices continue to drift out over time, consistent with dissipative dynamics of single vortices [67].

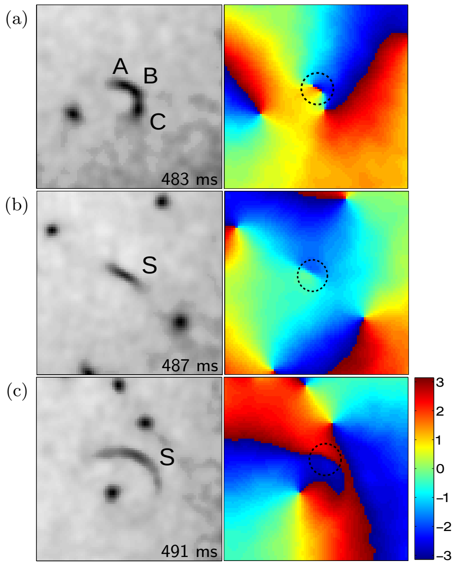

Our decomposition of N_v enables us to independently fit the drift and annihilation decay processes (as two coupled ODEs for N_d and N_a, equivalent to Eq. (6.2)), with the results shown in Fig. 6.4(c) and (d). In the absence of dissipation, we find $\Gamma_2 = 0.0040$ (It is not appropriate to discuss Γ_1 since $N_d(t)$ is not of a decaying form). While the experimental observations [59] suggest Γ_2 is proportional to T^2 and thus approaches 0 as $T \to 0$, our results demonstrate a finite Γ_2 in this limit. In the presence of dissipation we obtain $\Gamma_1 = 0.093$ and $\Gamma_2 = 0.0041$, which are comparable to the coldest experiments of Kwon *et al.*

Figure 6.5: Density (left) and phase (right) just before (a), immediately following (b) and a later time after (c) a vortex-antivortex annihilation event. The field of view is $[23.5\mu\text{m}]^2$, centered on the vortex pair/sound pulse (highlighted by a circle in the phase).

6.3.3 Crescent-Shaped Density Structures

In the experiment, Kwon *et al.* observed the occasional appearance of crescent-shaped waves of depleted density. Lacking direct access to the vortex signs, they suggested that these structures result from annihilation events of vortices of opposite circulation [70, 71, 72]: a vortex reconnection is predicted to induce an intense, localised, rarefaction sound pulse [73, 74]. Figure 6.5 shows snapshots of the condensate density and phase during a reconnection event. Vortices show up as localized dips in the density (left column) and 2π-defects in the phase (right column). Figure 6.5 (a) shows a vortex (A) and antivortex (B) close to each other, and a third vortex (C) in the vicinity. Note that the individual vortices are not spatially resolvable through their density alone (the vortex cores merge into a deep, elongated crescent-shaped depression), but they are clearly identified by the phase plot. A short time later (b), vortices A and B annihilate, as confirmed by the disappearance of their phase singularities, leaving behind a shallow rarefaction pulse (S) with a linear phase step. This pulse rapidly evolves into a shallow, crescent-shaped sound wave [Fig. 6.5 (c)]. In other words, our simulations yield crescent-shaped density features as seen in the experiment, but these features are not uniquely formed by annihilation events - they may also result from from two (or more) vortices in close proximity. Information about the condensate phase is thus crucial to distinguish the nature of these observed structures. In this direction, an approach has recently been proposed for the experimental detection of quantized vortices and their circulation in a 2D BEC [75].

6.3.4 Vortex Generation via an Elliptical Obstacle

It is evident from the snapshots in Figure 2 that the initial translation of the condensate past the obstacle generates not just vortices but also shape excitations, sound waves (low-amplitude density waves), and high-amplitude density waves. These additional excitations will heat the condensate and modify the subsequent turbulent dynamics in a highly nonlinear and complicated manner. While reducing the translational speed reduces this disruption, this also reduces the number of vortices. A less disruptive and more efficient (higher rate of vortex nucleation) means to generate vortices may be provided by employing a laser-induced obstacle with *elliptical*, rather than circular, cross-section (attainable through cylindrical beam focusing). Repeating our simulations with such an elliptical obstacle $V_{\rm obs}(x, y) = V_0 \exp\left[-2(\epsilon^2 x^2 + y^2)/d^2\right]$ with arbitrary ellipticity $\epsilon = 3$ (the short/long axis being parallel/perpendicular to the flow) confirms the same qualitative behaviour as for homogeneous systems [69]: the ellipticity acts to reduce the critical superfluid velocity and, for a given flow speed, increase the rate of vortex nucleation. To illustrate the merits of the elliptical obstacle, in Fig. 6 we depict snapshots of the condensate dynamics for ellipticity $\epsilon = 3$ and a translational speed of $v = 0.8$mm/s. Despite a lower translational speed, the number of vortices generated by the time the obstacle is removed is almost identical to the circular example of Fig. 3. As a consequence of the reduced translational speed, the condensate disruption is visibly reduced. It is also worth noting that the elliptical obstacle promotes the formation of clusters of like-signed vortices (see intermediate time), and thus may facilitate future exploration of coherent vortex structures.

6.4 Conclusion

In conclusion, we have shown that the recent experimental creation and decay of vortices within a BEC [59] is well described by simulations of the 2D GPE with phenomenological dissipation (despite the 3D nature of the system). Theoretical access to the condensate phase, and thus the circulation of the vortices, promotes our understanding of the dynamics. In the early stages of translation of the obstacle, a quasi-classical wake of vortices

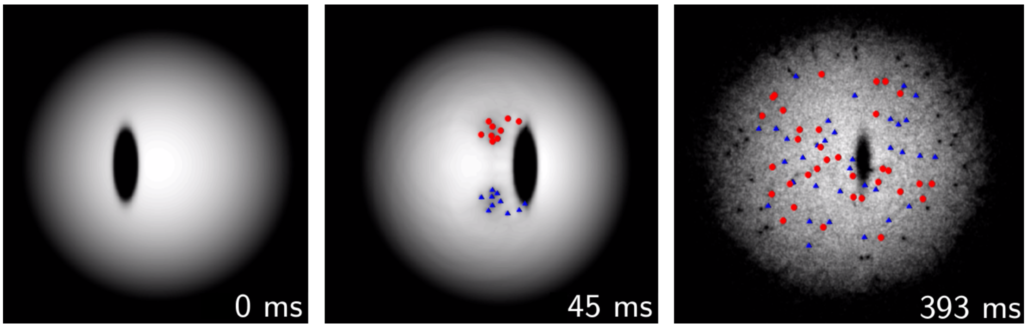

Figure 6.6: (Color online) Snapshots of the condensate density for a translational of speed v = 0.8mm/s past an elliptical obstacle (ellipticity $\epsilon = 3$). The field of view in each subfigure is of size $[170\mu\text{m}]^2$ and shifted along the x-axis so as to best display the condensate. Compared to the corresponding snapshots in Figure 2, the elliptical obstacle generates as many final vortices but at a lower translational speed and with reduced condensate disruption.

forms behind it, before symmetry breaking causes disorganisation of the vortices. After the obstacle is removed, the vortices decay in a manner which is both qualitatively and quantitatively consistent with the two mechanisms proposed by Kwon *et al.*, i.e. loss of vortices at the condensate edge due to thermal dissipation and vortex-antivortex annihilation events within the condensate. We confirm the occasional appearance of crescent-shaped density features, resulting either from the proximity of vortex cores or from a sound pulse which follows a vortex-antivortex reconnection. Finally, we propose that a moving *elliptical* obstacle may provide a cleaner and more efficient means to generate two-dimensional quantum turbulence.

Chapter 7

Critical velocity at finite temperature

7.1 Introduction

A defining feature of superfluids is the spontaneous formation of excitations when the flow exceeds a critical velocity relative to some obstacle or boundary, marking the breakdown of superfluid transport and the onset of dissipation. This can be understood in terms of the Landau criterion, which predicts excitations when the local fluid velocity exceeds $v_{\mathrm{L}} = \min[E(p)/p]$, where p is the momentum of elementary excitations and $E(p)$ their energy [42]. In weakly-interacting atomic Bose-Einstein condensates, $v_{\mathrm{L}} = c$, the speed of sound. The breakdown of superfluidity has been experimentally probed by introducing a localized repulsive obstacle, engineered via the repulsive force generated by focussed blue-detuned laser beam, and moving the condensate relative to the obstacle [40, 59, 76, 77, 37, 38, 39, 78]. This has enabled measurement of the critical velocity and the direct observation of the ensuing excitations, that is, pairs of quantized vortex lines with opposite polarity. In flattened condensates, this scenario is providing a route to engineer states of two-dimensional quantum turbulence [40, 59]. This scenario is also providing insight into the deep link between quantum fluids and their classical counterparts, where it has been predicted that the wake of quantized vortices produced downstream of the obstacle can collectively mimick the classical wakes, including the Bérnard-von Ká rmán vortex street [21, 69].

The motion of an obstacle in the zero-temperature Bose gas, described by the Gross-Pitaevskii equation, is a well-studied problem, particularly for circular obstacles in 2D geometries. The pioneering simulations by Frisch *et al.* [20] of an inpenetrable circular obstacle moving within the 2D nonlinear Schrödinger equation (NLSE), demonstrated a critical velocity of $v_{\mathrm{c}} \sim 0.4c$, above which vortex-antivortex pairs are nucleated. For small obstacles, boundary effects tend to suppress vortex nucleation, and as the size increases the critical velocity reduces towards an aymptotic value [29, 30, 31]). The critical velocity also depends on the shape of the obstacle, for example, obstacles with elliptical cross-section lead to reduced/heightened v_c, depending on the orientation relative to the flow [69, 79]. Similar behaviour holds for spherical obstacles, albeit with the emission of vortex rings and increased critical speeds of circa $0.7c$ [80, 43, 69]. In current condensate experiments [40, 59, 37, 38, 39, 78, 76, 77], the obstacles are penetrable, corresponding to a Gaussian potential of finite amplitude, produced via an incident blue-detuned laser beam. The same qualitative behaviour emerges as for the impenetrable obstacle, although the critical velocity and vortex nucleation patterns become modified [21].

Very recently, Kwon *et al.* undertook a systematic experimental analysis of the critical velocity for vortex shedding, exploring the dependence on the height and width of the penetrable obstacle, and the crossover from penetrable to impenetrable obstacles [76]. Their results, obtained in a condensate with a temperature much lower than the critical temperature for condensation, were found to be in agreement with previous zero-temperature predictions based on the Gross-Pitaesvkii equation. This work has made a significant step in consolidating our theoretical and experimental understanding of the critical velocity in a condensate in the zero-temperature limit. At the same time, it highlighted the scope to need to extend our understanding of the critical velocity to finite temperatures. While the role of finite temperature has been explored considerably for vortex nucleation in rotating systems, both experimentally [81, 82] and theoretically [83, 84, 85, 86], there is a paucity of literature relating to a linearly-translating obstacle. Indeed, to our knowledge, the only finite-temperature analysis of a moving obstacle in a condensate is that of Leadbeater *et al.*, who found that the critical velocity of a hard sphere decreased with temperature [87]. In this work we study the motion of a cylindrical Gaussian-shaped obstacle through a three-dimensional homogeneous Bose gas at finite temperature via classical field simulations. Above the critical velocity, vortex nucleation occurs either through pairs of vortex lines or collections of vortex rings. The critical velocity decreases with temperature and increases with condensate fraction. Indeed, the critical velocity is found to be closely proportional to the speed of sound of the condensate, which scales as the square root of the condensate fraction. In addition, we shed new light on the self-evolution of the non-equilbrium Bose gas, showing that the ensuing turbulent vortex tangle has the characteristics of Viven or ultra-quantum turbulence of a random vortex tangle, with a vortex line density which scales with the inverse of time.

7.2 Classical Field Method

We consider a weakly-interacting Bose gas with N atoms in a periodic box of volume ℓ^3. The atoms have mass m and their interactions are approximated by a contact pseudo-potential $V(\mathbf{r}-\mathbf{r}') = g\delta(\mathbf{r}-\mathbf{r}')$, where g is a coefficient which characterises the atomic interactions and δ denotes the Dirac delta function.

In order to theoretically model thermal excitations of the weakly-interacting Bose gas, one must progress beyond the standard mean-field approximation to a model which describes both the conden- sate and the thermal atoms in the gas. Various methods exist for this purpose, as reviewed elsewhere [88, 89, 90, 91, 92]. One of the most common is the classical field method [93, 94, 95, 96, 97, 98, 88]. This method is based on the observation that, providing the modes of the gas are highly occupied, then the gas is approximated by a classical field $\psi(\mathbf{r}, t)$ whose equation of motion is the Gross-Pitaevskii equation. However, whereas the Gross-Pitaevskii equation (GPE) conventionally describes the condensate only, $\psi(\mathbf{r}, t)$ now describes the entire multi-mode 'classical' gas [89, 91]. This method has been used to model diverse beyond-mean-field effects, including thermal equilibration dynamics [96, 98, 99, 100], condensate fractions [94], critical temperatures [101], correlation functions [102], spontaneous production of vortex-antivortex pairs in quasi-2D gases [103], thermal dissipation of vortices [104], and related effects in binary condensates [105, 106, 99].

Assuming high mode occupation, we parameterize the gas by the classical field $\psi(\mathbf{r}, t)$. The density distribution of atoms follows as $|\psi(\mathbf{r}, t)|^2$. The dynamics of ψ is governed by the Gross-Pitaevskii equation (GPE), which we write in dimensionless form as,

$$i\hbar \frac{\partial \psi}{\partial t} = \left(-\frac{\hbar^2}{2m} \nabla^2 + V(\mathbf{r}, t) + g \left| \psi \right|^2 \right) \psi. \tag{7.1}$$

$V(\mathbf{r}, t)$ denotes the externally applied potential. The GPE conserves the total number of particles $N = \int |\psi|^2 \, \mathrm{d}V$ and the total energy,

$$H = \int \left(\frac{\hbar^2}{2m} |\nabla \psi|^2 + \frac{g}{2} |\psi|^4 \right) \, \mathrm{d}V.$$

In what follows we will express quantities in terms of the natural units of the homogeneous Bose gas: density in terms of a uniform value ρ, length in terms of the healing length $\xi = \hbar/\sqrt{mg\rho}$, speed in terms of the speed of sound $c = \sqrt{\rho g/m}$, energy in terms of the chemical potential of the homogeneous condensate $\mu = \rho g$, and time in terms of $\tau = \hbar/g\rho$.

We label the modes of the system through the wavevector $\mathbf{k}$, and denote the mode occupation as $n_{\mathbf{k}}$. To allow for occupation across all classical modes of the system, the initial condition is highly non-equilibrium,

$$\psi\left(\mathbf{r}, t = 0\right) = \sum_{\mathbf{k}} a_{\mathbf{k}} \exp(i\mathbf{k} \cdot \mathbf{r}) \tag{7.2}$$

where the magnitudes of $a_{\mathbf{k}}$ are uniform and the phases are distributed randomly [96].

The GPE is evolved numerically, in the absence of any potential V, using a fourth-order

	Initial conditions					
N/ℓ^3 (ξ^{-3})	0.50	0.50	0.50	0.50	0.50	0.50
$\langle H\rangle/\ell^3$ ($\mu\xi^{-3}$)	2.57	2.13	1.75	1.33	0.53	0.23
	Equilibrium state					
ρ_0/ρ	0.02	0.22	0.36	0.48	0.77	0.91
T/T_λ	0.98	0.81	0.68	0.56	0.26	0.10

Table 7.1: Condensate fraction and temperature of the equilibrium classical field state for our chosen initial conditions.

Runge-Kutta method on a 192^3 periodic grid with time step $\Delta t = 0.01\tau$ and isotropic grid spacing $\Delta = 0.75\xi$. This spatial discretization implies that high momenta are not described; to formalize this effect, an ultraviolet cutoff is introduced, $n_{\mathbf{k}}(t) = 0$ for $k > 2\sqrt{3}\pi/\Delta$, where $k = |\mathbf{k}|$.

7.3 Equilibration dynamics and decay of the vortex tangle

The ensuing evolution from the strongly nonequilibrium initial conditions has been outlined previously [96, 99]. Initially the mode occupation numbers n_k are uniformly distributed over wavenumber k, up to the cutoff. Self-ordering leads to the rapid growth in the occupation of low-k modes, which initially evolves in a state of weak turbulence. The distribution evolves to a bimodal form. The high-k part of the distribution is associated with the thermal excitations and low mode occupations. The low-k part of the field is the quasi-condensate, characterised by macroscopic mode populations and superfluid ordering. The quasi-condensate is formed featuring a tangle of quantized vortices. Over very long times, this tangle relaxes. The true condensate is identified as the $k = 0$ mode, with condensate fraction ρ_0/ρ. The final equilibrium state, including its final condensate fraction and temperature, is free of superfluid vortices and uniquely determined by the number of particles N and the kinetic energy $E = \int(\hbar^2/2m)|\nabla\psi|^2\,\mathrm{d}V$ of the system [98].

Here we parameterise the system in terms of its particle density $\rho = N/\ell^3$ and average energy density $\langle H\rangle/\ell^3$. Note that the total energy $H = E + E_0$, where E is the kinetic energy of the system and E_0 is the energy of the condensate [98]. We determine the condensate fraction numerically from the population of the $k = 0$ mode. The temperature is subseqently evaluated from the condensate fraction using the empirical relationship established in Ref. [104],

$$\frac{T}{T_\lambda} = 1 - (1 - \alpha\sqrt{\rho})\frac{\rho_0}{\rho} - \alpha\sqrt{\rho}\left(\frac{\rho_0}{\rho}\right)^2, \tag{7.3}$$

where T_λ is the critical temperature for condensation and $\alpha = 0.2275$ is a fitting parameter. Table 7.1 shows the system parameters we employ in this work and the resulting condensate fractions and temperatures of the ensuing equilibrium classical field states.

We can visualize the slow equilibration process through the quasi-condensate itself. A quasi-condensate wavefunction $\hat{\psi}$ is defined by filtering and suppressing high-frequency spatial modes by transforming the complex amplitudes via $\hat{a}_{\mathbf{k}} = a_{\mathbf{k}} \times \max\{1 - k^2/k_c^2, 0\}$, as performed in Ref. [96]. The cutoff wave number, k_c, is chosen so as to include the entire quasi-condensate and minimal thermal modes, and estimated based on the bimodal disbtribution of the mode occupation numbersn_k. Thus $\hat{\psi}$ represents the long-wavelength component of the classical field. Here we take $k_c \approx 10\ \xi^{-1}$, although our qualitative results are insensitive to deviations in k_{c}.

Figure 7.1 shows the typical evolution of the quasi-condensate during the equilibration dynamics through iso-surface plots of the quasi-condensate density $|\hat{\psi}|^2$. The iso-surface density value ($0.04\,\langle|\hat{\psi}|^2\rangle$) is sufficiently low that only vortex cores are evident. The initially-formed dense vortex tangle relaxes over time. It remains random and isotropic throughout. Typically, the tangle relaxes to leave one or more vortex rings, which also relax, eventually leading to a vortex-free state. This is deemed the “equilibrated" state.

We can further analyse the vortex relaxation through the evolution of the vortex line-length density, L. It is convenient to evaluate the total vortex line length in terms of the total length of the isosurface tubes. We assume that each tube has uniform circular cross-sectional area A_{t}, measured by inspection of a given vortex line. Note that the assumption of uniform cross-section will be valid for the majority of vortex line length, but will deviate slightly where two vortices approach each other. The total tube length (viz. vortex line length) is then $V_{\mathrm{t}}/A_{\mathrm{t}}$, where V_{t} is the total tube volume.

The characteristic time of the evolution of the vortex tangle is $R^2/\ln(R/a_0)$, depending on the typical inter-vortex spacing, R, and the core size a_0 [107]. As the tangle dissipates the inter-vortex spacing increases, and so although most vortices dissipate at early times, for relatively large boxes, it can take a very long time for every single vortex to dissipate and the condensate to reach the equilibrium state. A sample of evolutions of the vortex volume during equilibration is shown in Figure 7.2. The tangle decay rate lies in reasonable agreement with the decay of a vortex tangle in a ‘random' Vinen state, with $L(t) \sim t^{-1}$.

7.4 Moving obstacle at finite-temperature

7.4.1 Set-up

Having obtained the equilibrated finite-temperature states of the Bose gas, we now move on to consider a laser-induced obstacle moving through the gas. The obstacle, uniform in z, is translated in the x-direction at speed v. Our simulations are conducted in the frame moving with the obstacle, modelled by the inclusion of a Galilean shift term $i\hbar v \partial_x \psi$ to the right-hand side of the GPE. In this frame the obstacle is imposed through the time-independent potential $V(\mathbf{r}) = V_0 \exp\left[-(x^2 + y^2)/d^2\right]$, where d and V_0 parameterize the

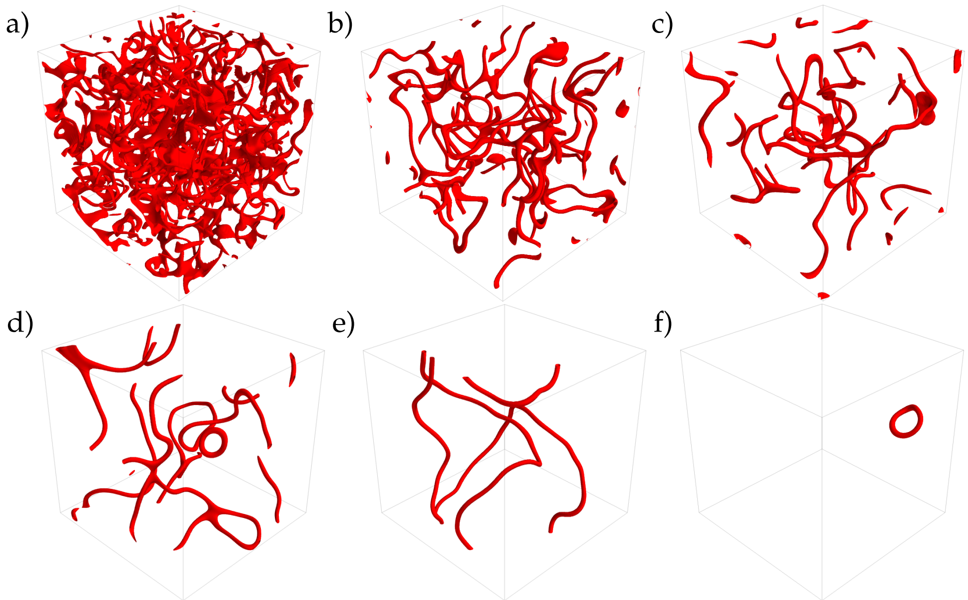

Figure 7.1: (Color online) Evolution of the quasi-condensate vortex tangle during the equilibration dynamics at times (a) $t/\tau = 0$, (b) 500, (c) 1000, (d) 2000, (e) 4000, and (f) 10 000. Shown are isosurfaces of the quasi-condensate density $|\hat{\psi}|^2 = 0.04\,\langle|\hat{\psi}|^2\rangle$. At later times all vortices disappear. Note that vortices cannot be visualized directly from the raw ψ due to the significant thermal fluctuations.

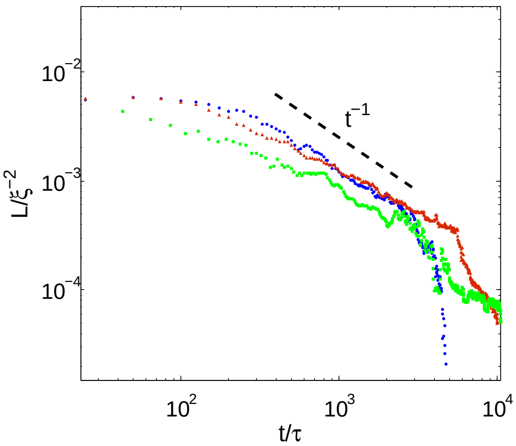

Figure 7.2: (Color online) Decay of the vortex line-length density during the equilibration dynamics, for various values of final condensate fraction: $\rho_0/\rho = 0.2$ (blue circles), $\rho_0/\rho = 0.5$ (brown triangles) and $\rho_0/\rho = 0.9$ (green squares)

width and amplitude of the potential. We employ a fixed amplitude $V_0 = 5\mu$. The frame speed is increased adiabatically to the required value according to the temporal profile $v\tanh(\hat{t}/200\tau)$, where $\hat{t}$ denotes the time from introduction of the obstacle.

7.4.2 Critical velocity

Simulations are repeated (from identical initial conditions) with increasing terminal speeds (in steps of $0.057c$) until vortices are observed to be nucleated from the obstacle (at an observation time of $\hat{t} = 500\tau$). This defines the critical velocity v_c.

Figure 7.3 shows the variation of v_c with both condensate fraction ρ_0/ρ (lower abscissa) and temperature T/T_λ (upper abscissa), for two example obstacles widths. The critical velocity has a maximum value at zero temperature (unit condensate fraction), and decreases nonlinearly as temperature increases (condensate fraction decreases), reaching zero at the critical point for condensation.

At zero temperature, the critical velocity is of the order of the condensate speed of sound $c = \sqrt{\rho g/m}$, with a general form $v_c(T = 0) = \beta c$, where β is a parameter which depends solely on the shape of the obstacle (here d and V_0). The simulated v_c data in Figure 7.3 closely follows a simple functional form given by $v_c(T) = v_c(T = 0)\sqrt{\frac{\rho_0}{\rho}}$, as shown by the dashed lines. Combining these forms, we can write a generalized form of the critical velocity, valid at zero and non-zero temperatures, as,

$$v_c(T) = \beta\sqrt{\frac{\rho_0 g}{m}}. \tag{7.4}$$

In other words, for a given obstacle, the critical velocity is a fixed ratio of the speed of sound based on the *condensate* density, rather than the total particle density [87].

The inset of Figure 7.3 shows the variation of v_c with the obstacle width d at finite temperature, for the example of $T/T_\lambda = 0.56$. The qualitative behaviour is consistent with that seen at zero temperature [26, 30, 69]: for small d the critical velocity is sensitive to d (due to the prominence of boundary layer effects) but as d increases v_c decreases towards a limiting values (the Eulerian limit). However, the critical velocities are systematically reduced compared to the zero temperature case due to the reduced condensate speed of sound at finite temperature.

7.4.3 Vortex nucleation

Finally we examine the manner in which vortices are nucleated from the obstacle. At zero temperature, one expects the nucleation of straight anti-parallel vortex lines from the obstacle, either released in unison or staggered in time [21, 69], and move downstream relative to the obstacle. Pairs of anti-parallel quantized are unstable to sinusoidal pertur-

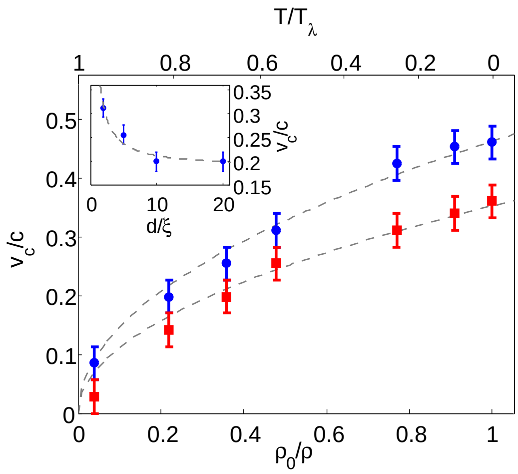

Figure 7.3: (Color online) Critical velocity v_c for the moving Gaussian-shaped obstacle (uniform in z) as a function of condensate fraction ρ_0/ρ and temperature T/T_λ, for obstacle widths $d = 2\xi$ (blue circles) and $d = 5\xi$ (red squares). The dotted lines show the analytic approximation $v_c = \beta\sqrt{\rho_0/\rho}$ with fitted coefficients $\beta = 0.46$ and 0.35. (Inset) The critical velocity approaches an asymptotic value as the obstacle size is increased. Included is a fit of the form $v_c = \alpha/d + \gamma$ with $\alpha = 0.26\ (\xi^2/\tau)$ and $\gamma = 0.18c$. Errors bars arise from the discretized values of v considered.

bations - the Crow instability - which grow over time, and may eventually lead to the lines reconnecting and generating vortex rings [108, 109, 74]. However, in the zero temperature case, this instability is very slow to manifest on a visible scale due to the high degree of parallelism of the vortex lines. Numerical simulations speed up the instability by imposing an initial perturbation on the vortex line, and the instability may be naturally sped up in an inhomogeneous condensate, where the vortex lines naturally deviate from straight lines.

We find two qualitative regimes of vortex nucleation at finite temperature. The first case is illustrated through the example in Fig. 7.4. A pair of “wiggly” vortex lines are nucleated from the obstacle, as seen in the final snapshot (iv). The wiggles are drive by the thermal fluctuations, which cause the vortex elements to be nucleated at slightly different times along the obstacle; this is visible at intermediate times (snapshots (iii) and (iv)). This regime of nucleation tends to occur for low speeds.

Figure 7.4(b) shows an example of the second regime of nucleation, which is characterised by the emission of vortex rings, rather than lines. This behaviour occurs for larger speeds. Again, the thermal fluctuations induce vortex nucleation at different times along the obstacle, but now the enhanced speed causes these localized vortex loops to peel away significantly from the obstacle, forming a series of vortex rings. At even higher speeds ($v/v_c \gg 1$), the frequency of vortex nucleation is large, with a significant interaction between successively-nucleated vortices. This leads to a complex tangle of vortex lines behind the obstacle.

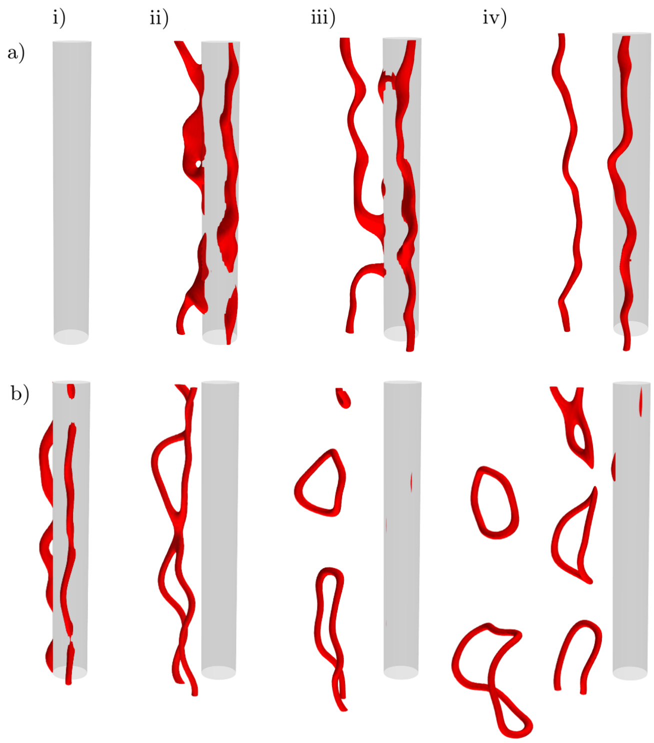

Figure 7.4: (Color online) Snapshots of the typical vortex nucleation from the moving Gaussian-shaped obstacle (gray) in the finite temperature Bose gas. Shown are isosurfaces of the quasi-condensate density ($|\hat{\psi}|^2 = 0.04\,\langle|\hat{\psi}|^2\rangle$). (a) Vortices are shed as pairs of anti-parallel vortex lines. Here the system parameters are $\rho_0/\rho = 0.2$ and $v = 0.17c$, and the snapshots correspond to times (i) $\hat{t}/\tau = 210$, (ii) 460, (iii) 585 and (iv) 710. (b) Vortex rings are nucleated from the obstacles. The system parameters are $\rho_0/\rho = 0.9$ and $v = 0.37c$, and the times are (i) $\hat{t}/\tau = 0$, (ii) 125, (iii) 250 and (iv) 500.

7.5 Conclusions

Using classical field simulations we have analysed the nucleation of vortices past a moving cylindrical obstacle in a finite temperature homogeneous Bose gas. We evolve the classical field from highly non-equilibrium initial conditions to thermalized equilibrium states with ranging temperatures and condensate fractions. During this evolution, the vortex tangle present in the quasi-condensate is shown to decay in accord with the Viven/ultraquantum form. A cylindrical obstacle with Gaussian profile is then introduced into the system, and the gas made to flow relative to the obstacle. Above the critical velocity, vortices are nucleated, either as wiggly anti-parallel pairs of vortex lines or as vortex rings. The critical velocity decreases with increasing temperature, becoming zero at the critical temperature, and scales with the speed of sound of the condensate, i.e. as the square root of the condensate fraction.

Chapter 8

Simulating the surface of a "Floppy Wire"

8.1 Superfluid wire experiments

Developments in flow visualization at very low temperatures [110, 111] have driven recent progress in the turbulence in superfluid ^{4}He and ^{3}He-B. Experiments and theory have highlighted effects such the existence of classical and nonclassical turbulent regimes [112], and energy transfer over length scales, both direct [113] and inverse [114, 115]. At the same time, improvements in the generation, observation and control of quantum vortices in atomic Bose–Einstein condensates[55, 116, 34, 58, 59] has added a character of interdisclinarity to the study of turbulence in quantum fluids.

In many superfluid helium experiments [117], turbulence is generated by moving grids [118], wires [119, 50, 120, 121, 19], forks [122, 123] or spheres [124]. Although macroscopically polished, the surface of these objects is rough on the length scale of the superfluid vortex core, which is of the order of 10^{-10} m in ^{4}He and 10^{-8} m in ^{3}He. As an example, Fig. 8.1(a) is an atomic force microscope (AFM) image showing the microscopic detail on the surface of a single–core NbTi 'floppy' wire used for generating superfluid turbulence [120]. Note the appearance of an elongated scratch, typical of such wires. No direct flow visualization is available on these microscopic length scales and, as such, superflow in the presence of walls remains poorly understood. In principle, the superfluid boundary conditions should be straighforward. In the simplest case of a boundary at rest, the superfluid velocity component which is perpendicular to the boundary must be equal to zero at the boundary, while the tangential component can slip. In practice, nucleation of quantum vorticity complicates this idealized Eulerian picture.

The established theoretical approaches used to successfully describe homogeneous superfluid turbulence away from boundaries can falter in the presence of realistic bound-

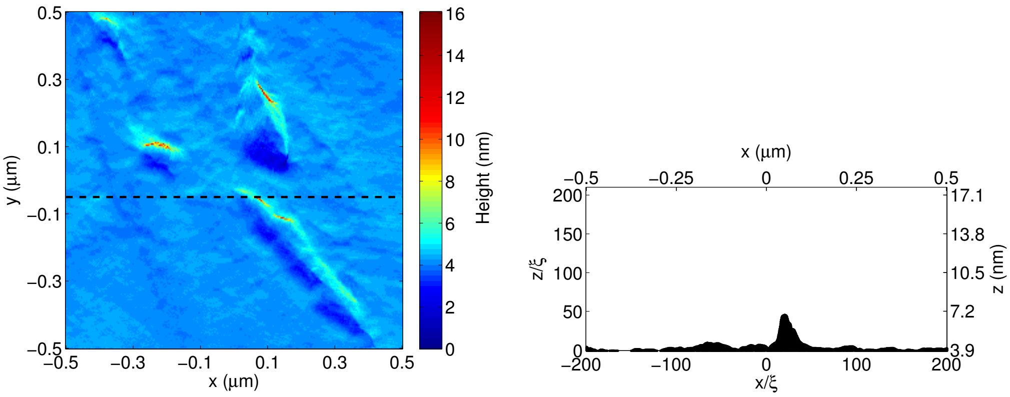

Figure 8.1: (a) AFM image of a typical NbTi wire used for the generation of quantum turbulence. The roughness of the surface is seen in the form of scratches along the surface. (b) The cross-section of the AFM data along $y = -0.05\mu$m (indicated by the dashed line in (a)) is imposed as a surface in our 2D simulations.

aries. First consider the vortex filament method of Schwarz [125, 126]. Its application to relatively simple and smooth boundaries, such as spheres [127, 128] and hemispheres [129], has proved cumbersome due to the complex system of images which is required. Its starting assumption, that the vortex core is infinitesimally smaller than any other length scale, makes it unsuitable for realistic boundaries of roughness comparable to the vortex core size. Moreover Schwarz's approach requires arbitrarily seeding vortex loops, because it does not account for vortex nucleation. Another approach which suffers similar difficulties [130] is the two–fluid Hall–Vinen–Bekarevich–Khalatnikov (HVBK) equations [131, 132]. Moreover, the HVBK equations are coarse–grained over length scales larger than the average vortex separation, hence the boundary conditions require further assumptions or the introduction of unknown sliding/pinning parameters.

A practical dynamical model of superflow near boundaries of arbitrary shape which is powerful enough to describe vortex nucleation is the Gross–Pitaevskii equation (GPE) [133]. While the GPE is an accurate quantitative description of atomic condensates, it provides only a qualitative model of superfluid helium. Frisch *et al.* pioneered the GPE approach by simulating superflow past a cylinder, observing vortex pair nucleation above a critical flow speed [20]. Subsequent GPE-based works have further elucidated vortex generation past a cylinder [23, 24, 21], as well as spheres and half-spheres [47], and elliptical objects [69]. Nevertheless, at this stage of investigation, the GPE is the optimum tool to gain physical insight into the flow of a superfluid over rough surfaces typical of experiments.

8.2 The "Floppy Wire" AFM image

8.3 GPE with AFM surface

8.4 2D clusters and backflow vortex generation

8.5 Theoretical Model

Within the GPE model the condensate is parameterized via a macroscopic wavefunction $\Psi(\mathbf{r}, t)$; this specifies the condensate (number) density $n(\mathbf{r}, t) = |\Psi(\mathbf{r}, t)|^2$. The GPE is

$$i\hbar\frac{\partial\Psi}{\partial t} = \left(-\frac{\hbar^2}{2m}\nabla^2 + V + g|\Psi|^2 + i\hbar v\frac{\partial\Psi}{\partial x} - \mu\right)\Psi. \tag{8.1}$$

where m is the mass of one atom, g is a coefficient that characterizes the atomic interactions, and μ is the chemical potential (energy per atom). $V(\mathbf{r}, t)$ is the external potential acting on the condensate; we will take this to represent the rough surface (see below). The speed-dependent term provides a Galilean transformation to a reference frame moving with speed v along x; this will enable us to model flow past the surface.

We express density in terms of the density at infinity n_0, energy in terms of μ, length in terms of the healing length $\xi = \hbar/\sqrt{mn_0g}$, and speed in terms of the sound speed $c = \sqrt{n_0g/m}$; our unit of time follows as $\tau = \xi/c$. In practice we solve the corresponding dimensionless GPE $i(\partial\Psi'/\partial t') = \left[-(1/2)\nabla^2 + V' + |\Psi'|^2 + iv(\partial\psi/\partial x) - 1\right]\Psi'$, where the prime indicates dimensionless quantities.

The AFM data depicted in Fig. 8.1(a) provides a two-dimensional map of the height of the surface, $z = h(x, y)$. We convert the z-scale into units of healing length using the value for ^{4}He, $\xi_4 = 0.66$Å[1]. Due to the lack of resolution in the x and y directions it is not possible to convert these on the scale of ξ_4; instead these directions are given arbitrary conversions into healing lengths with the range $-0.5\mu\text{m} \leq x, y \leq 0.5\mu\text{m}$ taken to be $-200\xi \leq x, y \leq 200\xi$, as shown in Fig. 8.1. To model the boundary through the external potential $V(x, y, z)$, we set $V = 0$ everywhere apart from below the surface, where we set $V = 50\mu$; this value is sufficiently large that it effectively contrains the density to zero.

Our numerical approach is to first obtain the stationary solution for the static fluid ($v = 0$), achieved via imaginary time propagation of the GPE [135]. From this initial condition the GPE is then propagated in real time, with the fluid speed v ramped up smoothly from zero up to its required value.

To assess the role of tall prominences in the surface, we will also consider cases where

[1]The vortex rings experiments of Rayfield & Reif [134] suggests a ^{4}He vortex core radius of around $a_0 = 1$Å. We define the vortex core in our simulations as the radius at which the density drops to 50% of the value at infinity, so $a_0 = 1.52\xi$. This gives us a $\xi = 1$Å$/1.52 \approx 0.66$Å for ^{4}He.

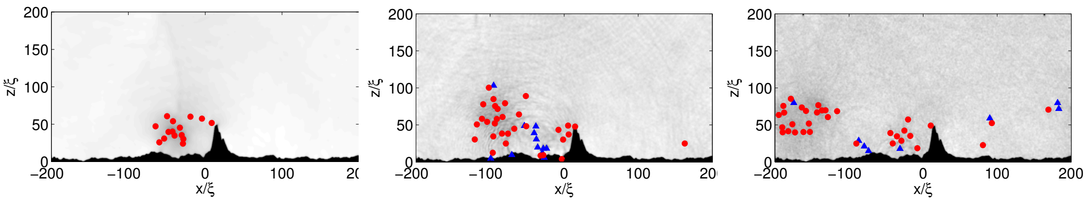

Figure 8.2: Evolution of 2D flow past the rough surface for a flow speed of $v = 0.35c$. Depicted are snapshots of density and vortex locations at times (from left to right) $t = 500$, 1580, and 2100 τ. Red (blue) circles represent vortices of positive (negative) circulation.

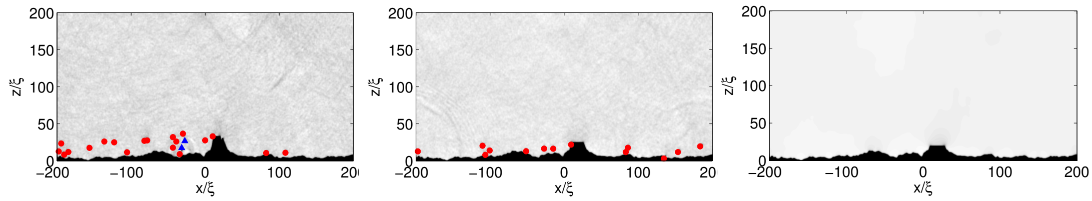

Figure 8.3: Same-time snapshots for various levels of surface truncation: (i) β = 70%, (ii) β = 50% and (iiii) β = 40%, where β represents the truncation height relative to the highest point in the surface. Depicted are snapshots of density and vortex locations. For comparison, the untruncated surface (β = 100%) is depicted in Fig. 8.2. The flow speed is $v = 0.35c$ and the time is $t = 2440\tau$.

the surface height $z = h(x, y)$ is truncated to a percentage β of the maximum height h_0, i.e. $h(x, y) \to h(x, y)H(z/h_0 = \beta)$, where $H(z)$ is the Heaviside step function (β = 100% corresponds to no truncation, $\beta = 0$ corresponds to complete truncation).

In 2D, we solve the (dimensionless) GPE using the 4th-order Runge–Kutta method, with periodic boundary conditions, on a 1024×512 grid with uniform spacing $\Delta = 0.4$. $y = -0.05\ \mu$m is used.

8.5.1 Typical Evolution

Superfluid flow past an obstacle at a velocity greater than a critical velocity causes vortices to be nucleated from the obstacle into the bulk of the fluid. For the rough surface we consider (Fig. 8.1) the prominences acts as obstacles. For simplicity we begin in 2D, modelling the flow past the surface depicted in Fig. 8.1(b). We find the critical velocity for vortex nucleation to be $v_c = (0.125 \pm 0.025)c$. We focus on an arbitrary super-critical flow speed of $v = 0.35c$, with Fig. 8.2 depicting the evolution of the system. For clarity we show both the condensate density (upper plots) and vortex locations/circulation (lower plots). At early times, a series of positive-circulation vortices (red) peel off from the peak of the large mountain. Vortices are nucleated here, and not elsewhere, due to the high curvature in the surface at this peak, which induces a relatively high local fluid velocity. As they are carried downstream the vortices stay in close proximity and co-rotate about one another; this leads to the vortices combining into a larger-scale cluster of positive circulation. This cluster travels downstream just above the surface. Close to the surface, the cluster introduces a large relative fluid flow in the positive-x direction. This interrupts the nucleation of vortices from the mountain top and also induces the secondary generation of vortices (blue) from smaller-scale surface prominences. These secondary vortices are of negative circulation and also form a vortex cluster. As this cluster grows, it leads to a cessation of secondary vortex production, and so again the primary vortices become nucleated from the mountain peak. This process repeats.

The total number of vortices N_v increases with time (Fig. 8.4(a), solid line); initially this increase is rapid but over time it slows down as the number of vortices within the finite-sized box begins to saturate. Initially this is almost entirely composed of positively-signed vortices (dashed line), apart from a small amount of spurious negative-sign vortices (dotted line). At $t \approx 700\tau$ the number of positive-sign vortices increases sharply; this represents the formation of secondary vortices.

It is important to note that the generation of secondary clusters requires the surface to be rough downstream of the mountain. If the surface is perfectly smooth downstream of the mountain, the positive-signed vortices persist.

Note also that it is possible for tertiary vortices/clusters of positive-sign; these arise when the secondary cluster induces a sufficiently high flow speed in the negative-x direction to generate vortices from the local surface roughness.

8.5.2 Truncated surfaces

It is evident above that the vortex generation is dominated by the large single prominence in the surface, with the smaller prominences having only a secondary effect. To further analysis this we next study how the flow is affected by truncation of the surface. Figure 8.3 shows a snapshot (at fixed time) for various levels of truncation β, with all cases having the same flow speed $v = 0.35c$. It is evident that the height of the mountain plays a critical role. Already, when the mountain is capped at 70%, the number of vortices produced by that time is vastly reduced. The vortices are generated at a sufficiently low frequency that only small clusters form; secondary vortices are still formed but in a much lower quantity. For $\beta = 50\%$ even fewer vortices are produced, and for this case no clustering takes place and in turn no secondary vortices are formed. For $\beta = 40\%$ no vortices are generated at all.

8.5.3 Dependence on flow speed

Figure 8.4(b) shows the final number of vortices as a function of the flow speed. For the three truncation levels considered, N_v is zero up to the critical velocity and then increases in an approximately linear manner.

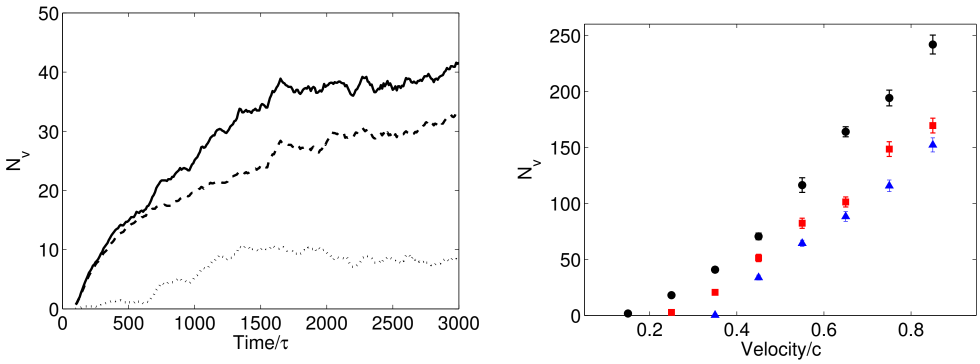

Figure 8.4: (a) Number of vortices produced during $v = 0.35c$ flow past the surface. Shown are the numbers of total vortices N_v (solid line), positive vortices (dashed line) and negative vortices (dotted line). (b) Final number of vortices N_v as a function of the flow velocity v for the 2d simulations. Each data point represents the average of 20 measurements of N_v in the vicinity of $t = 3000\tau$.

8.6 3D boundary layer and velocity statistics

Appendix A

Detailed Derivations

A.1 Derivation of the forth order Runge-Kutta equation

A.2 Derivation of the Hydrodynamic Equations via the Madelung Transformation

Inserting the Madelung transformation (Section 2.6) into the GPE and writing the result in tensor notation yields

$$\mathrm{i}\hbar\left(\frac{\partial R}{\partial t}+\mathrm{i}\frac{\partial \theta}{\partial t}R\right)e^{\mathrm{i}\theta}=-\frac{\hbar^2}{2m}e^{\mathrm{i}\theta}\left(\frac{\partial^2 R}{\partial x_j^2}+2\mathrm{i}\frac{\partial \theta}{\partial x_j}\frac{\partial R}{\partial x_j}+\mathrm{i}\frac{\partial^2 \theta}{\partial x_j^2}R-\frac{\partial \theta}{\partial x_j}\frac{\partial \theta}{\partial x_j}R\right)+gR^3e^{\mathrm{i}\theta}+VRe^{\mathrm{i}\theta}.$$

The real and imaginary parts of the GPE, once divided by $\exp(\mathrm{i}\theta)$, then take the form

$$-\hbar R\frac{\partial \theta}{\partial t}=-\frac{\hbar^2}{2m}\left(\frac{\partial^2 R}{\partial x_j \partial x_j}-R\frac{\partial \theta}{\partial x_j}\frac{\partial \theta}{\partial x_j}\right)+gR^3+VR, \tag{A.1}$$

$$\hbar\frac{\partial R}{\partial t}=-\frac{\hbar^2}{2m}\left(2\frac{\partial \theta}{\partial x_j}\frac{\partial R}{\partial x_j}+R\frac{\partial^2 \theta}{\partial x_j \partial x_j}\right). \tag{A.2}$$

Consider Equation (A.2) and note that $\rho=mR^2 \Rightarrow \frac{\partial \rho}{\partial t}=2mR\frac{\partial R}{\partial t}$, allowing us to rewrite the equation in terms of ρ,

$$\begin{aligned}\frac{\partial \rho}{\partial t}&=-\hbar R\left(2\frac{\partial \theta}{\partial x_j}\frac{\partial R}{\partial x_j}+R\frac{\partial^2 \theta}{\partial x_j \partial x_j}\right)\\&=-2mR\frac{\partial R}{\partial x_j}\frac{\partial}{\partial x_j}\left(\frac{\hbar}{m}\theta\right)-mR^2\frac{\partial^2}{\partial x_j \partial x_j}\left(\frac{\hbar}{m}\theta\right)\\&=-\frac{\partial \rho}{\partial x_j}\frac{\partial}{\partial x_j}\left(\frac{\hbar}{m}\theta\right)-\rho\frac{\partial^2}{\partial x_j \partial x_j}\left(\frac{\hbar}{m}\theta\right).\end{aligned}$$

The terms containing the phase can then be directly replaced with the fluid velocity, $v_j = \frac{\partial}{\partial x_j}\left(\frac{\hbar}{m}\theta\right)$.

$$\begin{aligned}\frac{\partial\rho}{\partial t} &= -\frac{\partial\rho}{\partial x_j}v_j - \rho\frac{\partial}{\partial x_j}v_j \\ &= -\frac{\partial}{\partial x_j}\left(\rho v_j\right).\end{aligned}$$

Rewritten in vector form the result is a continuity equation,

$$\frac{\partial\rho}{\partial t} + \nabla(\rho\mathbf{v}) = 0. \tag{A.3}$$

Now consider Equation (A.1), written in the form

$$\frac{\hbar}{m}\frac{\partial\theta}{\partial t} = \frac{\hbar^2}{2m^2}\left(\frac{1}{R}\frac{\partial^2 R}{\partial x_j\partial x_j} - \frac{\partial\theta}{\partial x_j}\frac{\partial\theta}{\partial x_j}\right) - \frac{gR^2}{m} - \frac{V}{m}.$$

Note that it can easily be shown $\frac{1}{R}\frac{\partial^2 R}{\partial x_j\partial x_j} = \frac{1}{\sqrt{\rho}}\nabla^2\sqrt{\rho}$ and $\frac{\hbar^2}{2m^2}\frac{\partial\theta}{\partial x_j}\frac{\partial\theta}{\partial x_j} = \frac{v^2}{2}$. It follows that Equation (A.1) can be written,

$$\begin{aligned}&\frac{\hbar}{m}\frac{\partial\theta}{\partial t} = \frac{\hbar^2}{2m^2}\frac{1}{\sqrt{\rho}}\nabla^2\sqrt{\rho} - \frac{v^2}{2} - \frac{gR^2}{m} - \frac{V}{m} \\ &\Rightarrow \frac{\partial}{\partial t}\left(\frac{\hbar}{m}\frac{\partial\theta}{\partial x_k}\right) = \frac{\partial}{\partial x_k}\left(\frac{\hbar^2}{2m^2}\frac{1}{\sqrt{\rho}}\nabla^2\sqrt{\rho}\right) - \frac{\partial}{\partial x_k}\left(\frac{v^2}{2}\right) - \frac{2gR}{m}\frac{\partial R}{\partial x_k} - \frac{1}{m}\frac{\partial V}{\partial x_k} \\ &\Rightarrow \rho\frac{\partial v_k}{\partial t} = \rho\frac{\partial}{\partial x_k}\left(\frac{\hbar^2}{2m^2}\frac{1}{\sqrt{\rho}}\nabla^2\sqrt{\rho}\right) - \rho\frac{\partial}{\partial x_k}\left(\frac{v^2}{2}\right) - 2gR^3\frac{\partial R}{\partial x_k} - \rho\frac{1}{m}\frac{\partial V}{\partial x_k}.\end{aligned}$$

By noticing that $p = \frac{1}{2}g\left(\frac{\rho}{m}\right)^2 = \frac{gR^4}{2}$ we can write $\frac{\partial p}{\partial x_k} = 2gR^3\frac{\partial R}{\partial x_k}$ and then,

$$\rho\frac{\partial v_k}{\partial t} + \rho\frac{\partial}{\partial x_k}\left(\frac{v^2}{2}\right) = \rho\frac{\partial}{\partial x_k}\left(\frac{\hbar^2}{2m^2}\frac{1}{\sqrt{\rho}}\nabla^2\sqrt{\rho}\right) - \frac{\partial p}{\partial x_k} - mR^2\frac{\partial}{\partial x_k}\left(\frac{V}{m}\right).$$

We now now use the following two results,

$$\begin{aligned}v_j\frac{\partial}{\partial x_j}v_k &= \frac{\partial}{\partial x_k}\left(\frac{v_jv_j}{2}\right) \\ 2\frac{\partial}{\partial x_k}\left(\frac{1}{\sqrt{\rho}}\frac{\partial^2}{\partial x_j\partial x_j}\sqrt{\rho}\right) &= \frac{1}{\rho}\frac{\partial}{\partial x_j}\rho\frac{\partial}{\partial x_j}\frac{\partial}{\partial x_k}\ln\rho,\end{aligned}$$

and find,

$$\rho\left(\frac{\partial}{\partial t}v_kv_j\frac{\partial v_k}{\partial x_j}\right) = -\frac{\partial p}{\partial x_k} - \frac{\partial}{\partial x_j}P_{jk} - \rho\frac{\partial}{\partial x_k}\left(\frac{V}{m}\right),$$

where $P_{jk} = -\frac{\hbar^2}{4m^2}\rho\frac{\partial^2 \ln\rho}{\partial x_j \partial x_k}$. Writing this in vector notation, we obtain an equation similar to the Euler equation for an inviscid fluid,

$$\rho\left(\frac{\partial \mathbf{v}}{\partial t} + (\mathbf{v}\cdot\nabla)\,\mathbf{v}\right) = -\nabla p - \nabla\mathbf{P} - \rho\nabla\left(\frac{V}{m}\right). \tag{A.4}$$

A.3 Derivation of the Gross-Pitaevskii Equation

This section derives the GPE following the methodology outlined in [NPP GPE tutorial]. We begin by revisiting the quantum field theory formalism used to describe a many body quantum system[Fetter 71]. Such a system is described by an N-body wavefunction, $\tilde{\Psi}(\mathbf{r}_1...\mathbf{r}_N, t)$ which obeys the famous Schrödinger equation

$$i\hbar\frac{\partial}{\partial t}\tilde{\Psi}(\mathbf{r}_1...\mathbf{r}_N, t) = \hat{H}\tilde{\Psi}(\mathbf{r}_1...\mathbf{r}_N, t), \tag{A.5}$$

where $\mathbf{r}_i$ describes the coordinates of the ith body. Consider a closed system containing a dilute, weakly interacting Bose gas of N atoms. Such a system would be described by $\tilde{\Psi}(\mathbf{r}_1...\mathbf{r}_N, t)$, with a Hamiltonian of the form

$$\hat{H} = \sum_{k=1}^{N}\hat{h}_0(\mathbf{r}_k, t) + \frac{1}{2}\sum_{k,l=1}^{N}\hat{V}(\mathbf{r}_k, \mathbf{r}_l). \tag{A.6}$$

Here $\hat{h}_0(\mathbf{r}, t) = -\frac{\hbar^2}{2m}\nabla^2 + V_{\text{ext}}(\mathbf{r}, t)$ is a contribution arising from the effects of a single particle in an external potential. We assume in the dilute gas all interactions are binary; and so the second term arises from collisions between 2 atoms. The factor of $\frac{1}{2}$ ensures the effects are only counted once over the entire sum.

We now reformulate this system in a different representation, using the so called 'occupation number' orthonormal basis $|n_1...n_\infty\rangle$. This basis arises from the observation that multiple particles sharing an energetically accessible state are indistinguishable. Instead we consider only the number of particles in each state i and denote this n_i. Such states often correspond to states with fixed energy ε_i. While the number of states are infinite, our system contains a fixed number of bosons, N, implying that there are at most N states occupied.

The wavefunction is mapped into the 'occupation number' basis via

$$\tilde{\Psi}(\mathbf{r}_1...\mathbf{r}_N, t) \rightarrow |\tilde{\Psi}(t)\rangle = \sum_{n_1...n_\infty} c(n_1...n_\infty, t)\,|n_1...n_\infty\rangle,$$

with appropriately chosen complex coefficients, $c(n_1...n_\infty, t)$. The values c must follow the particle statistics rules (e.g. for Bosons much be symmetric under swapping of quantum numbers) and be normalised so that the probabilities correctly sum to one. We find that for our bosons,

$$\int |\tilde{\Psi}|^2 \, d\mathbf{r} = 1 \Rightarrow \sum_{n_1 \ldots n_\infty} |c(n_1 \ldots n_\infty, t)|^2 \frac{N!}{n_1! \ldots n_\infty!} = 1.$$

In this formulation, note that the state vectors $|n_1 \ldots n_\infty\rangle$ are time-independent, and the evolution of the system is entirely encoded in the values of $c(n_1 \ldots n_\infty, t)$. As part of the overall picture, we also must describe the movement of bosons between different states or energy levels. It is convenient to visualise this as the simultaneous destruction of a particle in state j and creation of a particle in state i, described mathematically using the single particle annihilation and creation operators[Shiff49].

$$\hat{a}_j \, |n_1 \ldots n_i \ldots n_j \ldots n_\infty\rangle = \sqrt{n_j} \, |n_1 \ldots n_i \ldots n_j - 1 \ldots n_\infty\rangle \, ,$$
$$\hat{a}_i^\dagger \, |n_1 \ldots n_i \ldots n_j \ldots n_\infty\rangle = \sqrt{n_i + 1} \, |n_1 \ldots n_i + 1 \ldots n_j \ldots n_\infty\rangle \, ,$$

which satisfy the bosonic commutation relations,

$$[\hat{a}_i, \hat{a}_j^\dagger] = \delta_{ij} \qquad [\hat{a}_i, \hat{a}_j] = [\hat{a}_i^\dagger, \hat{a}_j^\dagger] = 0.$$

Any single particle changing states can now be described through these operators; a particle moving from state j to state i is described using a single annihilation operator and a single creation operator through the product $\hat{a}_i^\dagger \hat{a}_j$. Similarly, as we decided to simplify the system by considering a dilute gas where all interactions are binary collisions, all interactions can be described by two particles changing state, using the product $\hat{a}_i^\dagger \hat{a}_k^\dagger \hat{a}_j \hat{a}_l$. Using these tools and ideas, the original description in Equations A.5 and A.6 is now written

$$i\hbar \frac{\partial}{\partial t} |\tilde{\Psi}\rangle = \hat{H} \, |\tilde{\Psi}\rangle \, ,$$

with the Hamiltonian

$$\hat{H} = \sum_{ij} \langle i| \, \hat{h}_0 \, |j\rangle \, \hat{a}_i^\dagger \hat{a}_j + \frac{1}{2} \sum_{ijkl} \langle ik| \, \hat{V} \, |jl\rangle \, \hat{a}_i^\dagger \hat{a}_k^\dagger \hat{a}_j \hat{a}_l, \tag{A.7}$$

where

$$\langle i| \, \hat{h}_0 \, |j\rangle = \int \phi_i^*(\mathbf{r}) \hat{h}_0 \phi_j(\mathbf{r}) \, d\mathbf{r},$$
$$\langle ik| \, \hat{V} \, |jl\rangle = \frac{1}{2} \left[(ik|\hat{V}|jl) + (ik|\hat{V}|lj) \right],$$
$$(ik|\hat{V}|jl) = \iint \phi_i^*(\mathbf{r}) \phi_k^*(\mathbf{r}') \hat{V}(\mathbf{r} - \mathbf{r}') \phi_l(\mathbf{r}') \phi_j(\mathbf{r}) \, d\mathbf{r}' d\mathbf{r}.$$

For further convenience we introduce the so called Bose field operators

$$\hat{\Psi}(\mathbf{r},t) = \sum_i \hat{a}_i(t)\phi_i(\mathbf{r},t),$$
$$\hat{\Psi}^\dagger(\mathbf{r},t) = \sum_i \hat{a}_i^\dagger(t)\phi_i(\mathbf{r},t),$$

which can be thought of as operators that represent the addition or removal of a particle at time t and location $\mathbf{r}$. As with the annihilation and creation operators, the Bose field operators also satisfy the commutation relations,

$$[\hat{\Psi}(\mathbf{r},t), \hat{\Psi}^\dagger(\mathbf{r}',t)] = \delta(\mathbf{r}-\mathbf{r}') \qquad [\hat{\Psi}(\mathbf{r},t), \hat{\Psi}(\mathbf{r}',t)] = [\hat{\Psi}^\dagger(\mathbf{r},t), \hat{\Psi}^\dagger(\mathbf{r}',t)] = 0. \tag{A.8}$$

Using these operators, the Hamiltonian in Equation A.7 can be again rewritten as

$$\begin{aligned}\hat{H} = &\int \hat{\Psi}^\dagger(\mathbf{r},t)\,\hat{h}_0\hat{\Psi}(\mathbf{r},t)\,d\mathbf{r} \\ &+ \frac{1}{2}\iint \hat{\Psi}^\dagger(\mathbf{r},t)\hat{\Psi}^\dagger(\mathbf{r}',t)V(\mathbf{r}-\mathbf{r}')\hat{\Psi}(\mathbf{r}',t)\hat{\Psi}(\mathbf{r},t)\,d\mathbf{r}'d\mathbf{r}.\end{aligned} \tag{A.9}$$

where, as before, $\hat{h}_0(\mathbf{r}_k,t) = -\frac{\hbar^2}{2m}\nabla^2 + V_{\text{ext}}(\mathbf{r},t)$ and $V(\mathbf{r}-\mathbf{r}')$ is the two body interaction potential.

We now add to our approximations a frequent simplification of the interaction potential and consider all interactions as totally elastic contact collisions. The strength of this interaction is usually taken to be $g = 4\pi\hbar^2 a/m$, where a is the s-wave scattering length, measured for a particular atom in the lab. Our two body interaction potential then becomes,

$$V(\mathbf{r}-\mathbf{r}') = g\delta(\mathbf{r}-\mathbf{r}'),$$

which when inserted into Equation A.9 gives the Hamiltonian,

$$\hat{H} = \int \hat{\Psi}^\dagger(\mathbf{r},t)\,\hat{h}_0\hat{\Psi}(\mathbf{r},t)\,d\mathbf{r} + \frac{g}{2}\int \hat{\Psi}^\dagger(\mathbf{r},t)\hat{\Psi}^\dagger(\mathbf{r},t)\hat{\Psi}(\mathbf{r},t)\hat{\Psi}(\mathbf{r},t)\,d\mathbf{r}.$$

The Bose field operator $\hat{\Psi}(\mathbf{r},t)$ evolves over time according to the Heisenberg equation of motion

$$i\hbar\frac{\partial}{\partial t}\hat{\Psi}(\mathbf{r},t) = [\hat{\Psi}(\mathbf{r},t), \hat{H}].$$

By expanding out the commutator, using standard commutator identities along with the relations in Equation A.8 and integrating out resulting delta functions we find

$$
\begin{aligned}
i\hbar\frac{\partial}{\partial t}\hat{\Psi}(\mathbf{r},t) &= \int [\hat{\Psi},\hat{\Psi}^{\dagger}\hat{h}_0\hat{\Psi}]\,d\mathbf{r} + \frac{g}{2}\int [\hat{\Psi},\hat{\Psi}^{\dagger}\hat{\Psi}^{\dagger}\hat{\Psi}\hat{\Psi}]\,d\mathbf{r} \\
&= \int [\hat{\Psi},\hat{\Psi}^{\dagger}]\hat{h}_0\hat{\Psi} + \hat{\Psi}^{\dagger}[\hat{\Psi},\hat{h}_0\hat{\Psi}]\,d\mathbf{r} \\
&\quad + \frac{g}{2}\int [\hat{\Psi},\hat{\Psi}^{\dagger}]\hat{\Psi}^{\dagger}\hat{\Psi}\hat{\Psi} + \hat{\Psi}^{\dagger}[\hat{\Psi},\hat{\Psi}^{\dagger}]\hat{\Psi}\hat{\Psi} + \hat{\Psi}^{\dagger}\hat{\Psi}^{\dagger}[\hat{\Psi},\hat{\Psi}\hat{\Psi}]\,d\mathbf{r} \\
&= \hat{h}_0\hat{\Psi}(\mathbf{r},t) + g\hat{\Psi}^{\dagger}(\mathbf{r},t)\hat{\Psi}(\mathbf{r},t)\hat{\Psi}(\mathbf{r},t).
\end{aligned}
\tag{A.10}
$$

We can continue to simplify the equation of motion by considering a mean-field approach for a single macroscopically occupied state. In the case of Bose-Einstein condensation the lowest energy level is macroscopically occupied and so we decompose the field operator via

$$\hat{\Psi}(\mathbf{r},t) = \hat{\psi}(\mathbf{r},t) + \hat{\delta}(\mathbf{r},t),$$

where $\psi(\mathbf{r},t)$ is a field operator for the condensate and $\hat{\delta}(\mathbf{r},t)$ is a field operator for the non-condensed atoms, whether that be atoms in higher states, atoms residing in the thermal cloud, or atoms influenced by quantum mechanical fluctuations.

We now make the Bogoliubov approximation [bogo47], a somewhat violent symmetry breaking approximation in which the condensate field operator is replaced by a classical field,

$$\hat{\psi}(\mathbf{r},t) = \psi(\mathbf{r},t) = \sqrt{N_0}\phi_0(\mathbf{r},t),$$

where N_0 is the number of particles in the condensate. Written in this way, it is then possible to approximate the condensate density using $n(\mathbf{r},t) = |\psi(\mathbf{r},t)|^2$. Unfortunately a direct consequence of the action is that the physical state described by $\hat{\Psi}(\mathbf{r},t)$ no longer satisfies the same symmetries as before. In particular, the total number of particles is not conserved. This approximation is justified by the understanding that as the condensate forms, it takes on a single phase, and all the particles in the condensate can be described by a single wavefunction. In addition, it is assumed that if there are many particles in the condensate, the exact value of N_0 does not affect the system state significantly, that is, $N_0 \approx N_0 + 1$. This approximation is essentially equivalent to the statement $\langle\hat{\Psi}(\mathbf{r},t)\rangle = \psi(\mathbf{r},t) \neq 0$, where $\langle\ldots\rangle$ denotes the ensemble average. The non-condensed field operator $\hat{\delta}(\mathbf{r},t)$ remains as an operator in the decomposition, and captures all the fluctuations around $\psi(\mathbf{r},t)$. It is generally assumed that $\langle\hat{\delta}(\mathbf{r},t)\rangle = 0$.

In principle, the classical field $\psi(\mathbf{r},t)$ is interpreted as the condensed atoms , however it can also be interpreted as the condensate atoms along with excitations of the system, as long as the occupation at high energy states $n_{i\gg1}$ and the size of quantum fluctuations are both negligible. The classical field, or c-field, approaches can be used to model finite temperature effects by modelling part of the thermal cloud with highly populated modes below a certain momentum cutoff [c-field citations].

In the limit of $T \to 0$, all of the particles become part of the condensate, so that $N = N_0$. The contribution from the non-condensate atoms can be neglected, $\hat{\delta}(\mathbf{r}, t) = 0$, and the field operator is written $\hat{\Psi}(\mathbf{r}, t) = \psi(\mathbf{r}, t)$. In this case, the Heisenberg equation of motion in Equation A.10 reduces to

$$\begin{aligned} i\hbar\frac{\partial}{\partial t}\psi(\mathbf{r}, t) &= \hat{h}_0\psi(\mathbf{r}, t) + g\psi^*(\mathbf{r}, t)\psi(\mathbf{r}, t)\psi(\mathbf{r}, t) \\ &= \left(-\frac{\hbar^2}{2m}\nabla^2 + V_{\text{ext}}(\mathbf{r}, t) + g|\psi(\mathbf{r}, t)|^2\right)\psi(\mathbf{r}, t), \end{aligned}$$

the the so called Gross-Pitaevskii equation (GPE), also known as the non-linear Schrödinger equation.

Finally, note that as the particle number is no longer strictly conserved, calculations should be performed within the grand canonical ensemble [Huang]. This approach leads to the modified Hamiltonian $\hat{H} \to \hat{H} - \mu\hat{N}$, where μ is the chemical potential and $\hat{N}$ is the total number operator. The above derivations can be easily repeated with the modified Hamiltonian to obtain a physically equivalent version of the GPE with a chemical potential term,

$$i\hbar\frac{\partial}{\partial t}\psi(\mathbf{r}, t) = \left(-\frac{\hbar^2}{2m}\nabla^2 + V_{\text{ext}}(\mathbf{r}, t) + g|\psi(\mathbf{r}, t)|^2 - \mu\right)\psi(\mathbf{r}, t). \tag{A.11}$$

A.4 Energy

A.5 Force

$$T_{jk} = \rho v_j v_k + p\delta_{jk} - \frac{\hbar^2}{4m^2}\rho\frac{\partial}{\partial x_j}\frac{\partial}{\partial x_k}\ln\rho \tag{A.12}$$

$$F_k = \frac{\partial}{\partial t}\int_V J_k \,\mathrm{d}V = -\int_V \frac{\partial}{\partial x_j}T_{jk}\,\mathrm{d}V - \int_V \rho\frac{\partial}{\partial x_k}\left(\frac{V}{m}\right)\mathrm{d}V \tag{A.13}$$

Bibliography

[1] A. Görlitz, J. M. Vogels, A. E. Leanhardt, C. Raman, T. L. Gustavson, J. R. Abo-Shaeer, A. P. Chikkatur, S. Gupta, S. Inouye, T. Rosenband, et al., Phys. Rev. Lett. **87**, 130402 (2001).

[2] W. H. Press, S. A. Teukolsky, W. T. Vetterling, and B. P. Flannery, *Numerical Recipes in FORTRAN; The Art of Scientific Computing* (Cambridge University Press, New York, NY, USA, 1993), 2nd ed., ISBN 0521437164.

[3] S. Taneda, J. Phys. Soc. Jpn. **11**, 302 (1956).

[4] S. Taneda, J. Phys. Soc. Jpn. **50**, 1398 (1981).

[5] M. Van Dyke, *An Album of Fluid Motion* (Parabolic Press, Stanford, CA, 1982).

[6] J. Maurer and P. Tabeling, EPL (Europhysics Letters) **43**, 29 (1998).

[7] J. Salort, C. Baudet, B. Castaing, B. Chabaud, F. Daviaud, T. Didelot, P. Diribarne, B. Dubrulle, Y. Gagne, F. Gauthier, et al., Physics of Fluids **22**, 125102 (2010).

[8] C. Nore, M. Abid, and M. E. Brachet, Phys. Rev. Lett. **78**, 3896 (1997).

[9] M. Kobayashi and M. Tsubota, Phys. Rev. Lett. **94**, 065302 (2005).

[10] A. W. Baggaley, J. Laurie, and C. F. Barenghi, Phys. Rev. Lett. **109**, 205304 (2012).

[11] JETP Letters **80**, 479 (2004).

[12] U. Frisch, *Turbulence. The legacy of A .N. Kolmogorov* (Cambridge University Press, Cambridge, 1995).

[13] C. F. Barenghi, V. L'vov, and P.-E. Roche, *Velocity spectra of quantum turbulence: experiments, numerics and models* (2013), `arXiv:1306.6248`.

[14] M. R. Smith, D. K. Hilton, and S. Van Sciver, Phys. Fluids **11**, 1 (1999).

[15] T. Zhang and S. Van Sciver, Nature Physics **1**, 36 (2005).

[16] Y. Sergeev and C. Barenghi, J. Low Temp. Phys. **157**, 429 (2009).

[17] R. Hänninen, M. Tsubota, and W. F. Vinen, Phys. Rev. B **75**, 064502 (2007).

[18] S. Fujiyama and M. Tsubota, Phys. Rev. B **79**, 094513 (2009).

[19] R. Goto, S. Fujiyama, H. Yano, Y. Nago, N. Hashimoto, K. Obara, O. Ishikawa, M. Tsubota, and T. Hata, Phys. Rev. Lett. **100**, 045301 (2008).

[20] T. Frisch, Y. Pomeau, and S. Rica, Phys. Rev. Lett. **69**, 1644 (1992).

[21] K. Sasaki, N. Suzuki, and H. Saito, Phys. Rev. Lett. **104**, 150404 (2010).

[22] B. Jackson, J. F. McCann, and C. S. Adams, Phys. Rev. A **61**, 051603 (2000).

[23] C. Nore, M. E. Brachet, and S. Fauve, Physica D **65**, 154 (1993).

[24] T. Winiecki, J. F. McCann, and C. S. Adams, Phys. Rev. Lett. **82**, 5186 (1999).

[25] T. Winiecki, B. Jackson, J. F. McCann, and C. S. Adams, Journal of Physics B: Atomic, Molecular and Optical Physics **33**, 4069 (2000).

[26] C. Huepe and M. E. Brachet, Physica (Amsterdam) **140**, 126 (2000).

[27] J. S. Stießberger and W. Zwerger, Phys. Rev. A **62**, 061601 (2000).

[28] M. Crescimanno, C. G. Koay, R. Peterson, and R. Walsworth, Phys. Rev. A **62**, 063612 (2000).

[29] N. G. Berloff and P. H. Roberts, J. Phys. A **33**, 4025 (2000).

[30] S. Rica, Physica D **148**, 221 (2001).

[31] C. T. Pham, C. Nore, and M. E. Brachet, Comptes Rendus Physique **5**, 3 (2004).

[32] B. Jackson, J. F. McCann, and C. S. Adams, Phys. Rev. Lett. **80**, 3903 (1998).

[33] K. Fujimoto and M. Tsubota, Phys. Rev. A **83**, 053609 (2011).

[34] T. Aioi, T. Kadokura, T. Kishimoto, and H. Saito, Phys. Rev. X **1**, 021003 (2011).

[35] G. A. El, A. Gammal, and A. M. Kamchatnov, Phys. Rev. Lett. **97**, 180405 (2006).

[36] I. Carusotto, S. X. Hu, L. A. Collins, and A. Smerzi, Phys. Rev. Lett. **97**, 260403 (2006).

[37] C. Raman, M. Köhl, R. Onofrio, D. S. Durfee, C. E. Kuklewicz, Z. Hadzibabic, and W. Ketterle, Phys. Rev. Lett. **83**, 2502 (1999).

[38] R. Onofrio, C. Raman, J. M. Vogels, J. R. Abo-Shaeer, A. P. Chikkatur, and W. Ketterle, Phys. Rev. Lett. **85**, 2228 (2000).

[39] S. Inouye, S. Gupta, T. Rosenband, A. P. Chikkatur, A. Görlitz, T. L. Gustavson, A. E. Leanhardt, D. E. Pritchard, and W. Ketterle, Phys. Rev. Lett. **87**, 080402 (2001).

[40] T. W. Neely, E. C. Samson, A. S. Bradley, M. J. Davis, and B. P. Anderson, Phys. Rev. Lett. **104**, 160401 (2010).

[41] R. J. Donnelly, *Quantized Vortices in Helium II* (Cambridge University Press, Cambridge, 1991).

[42] P. Nozières and D. Pines, *The Theory of Quantum Liquids II* (Addison-Wesley, Redwood City, 1990).

[43] T. Winiecki, Ph.D. thesis, The University of Durham (2001).

[44] A. C. White, C. F. Barenghi, and N. P. Proukakis, Phys. Rev. A **86**, 013635 (2012).

[45] M. T. Reeves, T. P. Billam, B. P. Anderson, and A. S. Bradley, Phys. Rev. Lett. **110**, 104501 (2013).

[46] A. W. Baggaley, C. F. Barenghi, A. Shukurov, and Y. A. Sergeev, EPL (Europhysics Letters) **98**, 26002 (2012).

[47] T. Winiecki, J. F. McCann, and C. S. Adams, EPL (Europhysics Letters) **48**, 475 (1999).

[48] D. H. Wacks, A. W. Baggaley, and C. F. Barenghi, Physics of Fluids **26**, 027102 (2014).

[49] M. Blažková, D. Schmoranzer, L. Skrbek, and W. F. Vinen, Phys. Rev. B **79**, 054522 (2009).

[50] D. I. Bradley, D. O. Clubb, S. N. Fisher, A. M. Guénault, R. P. Haley, C. J. Matthews, G. R. Pickett, V. Tsepelin, and K. Zaki, Phys. Rev. Lett. **95**, 035302 (2005).

[51] C. J. Foster, P. B. Blakie, and M. J. Davis, Phys. Rev. A **81**, 023623 (2010).

[52] A. C. White, B. P. Anderson, and V. S. Bagnato, Proceedings of the National Academy of Sciences **111**, 4719 (2014).

[53] C. F. Barenghi, L. Skrbek, and K. R. Sreenivasan, Proceedings of the National Academy of Sciences **111**, 4647 (2014).

[54] C. F. Barenghi, R. Donnelly, W. Vinen, and eds., *Quantized Vortex Dynamics and Superfluid Turbulence* (Springer, Berlin, 2001).

[55] E. A. L. Henn, J. A. Seman, G. Roati, K. M. F. Magalhães, and V. S. Bagnato, Phys. Rev. Lett. **103**, 045301 (2009).

[56] N. G. Parker and C. S. Adams, Phys. Rev. Lett. **95**, 145301 (2005).

[57] S. Middelkamp, P. J. Torres, P. G. Kevrekidis, D. J. Frantzeskakis, R. Carretero-González, P. Schmelcher, D. V. Freilich, and D. S. Hall, Phys. Rev. A **84**, 011605 (2011).

[58] T. W. Neely, A. S. Bradley, E. C. Samson, S. J. Rooney, E. M. Wright, K. J. H. Law, R. Carretero-González, P. G. Kevrekidis, M. J. Davis, and B. P. Anderson, Phys. Rev. Lett. **111**, 235301 (2013).

[59] W. J. Kwon, G. Moon, J.-y. Choi, S. W. Seo, and Y.-i. Shin, Phys. Rev. A **90**, 063627 (2014).

[60] A. M. Mateo and V. Delgado, Phys. Rev. A **74**, 065602 (2006).

[61] N. G. Parker and D. H. J. O'Dell, Phys. Rev. A **78**, 041601 (2008).

[62] B. Jackson, N. P. Proukakis, C. F. Barenghi, and E. Zaremba, Phys. Rev. A **79**, 053615 (2009).

[63] Y. Shin, private communication.

[64] S. Choi, S. A. Morgan, and K. Burnett, Phys. Rev. A **57**, 4057 (1998).

[65] M. Tsubota, K. Kasamatsu, and M. Ueda, Phys. Rev. A **65**, 023603 (2002).

[66] E. Madarassy and C. F. Barenghi, Journal of Low Temperature Physics **152**, 122 (2008).

[67] A. J. Allen, E. Zaremba, C. F. Barenghi, and N. P. Proukakis, Phys. Rev. A **87**, 013630 (2013).

[68] D. Yan, R. Carretero-González, D. J. Frantzeskakis, P. G. Kevrekidis, N. P. Proukakis, and D. Spirn, Phys. Rev. A **89**, 043613 (2014).

[69] G. W. Stagg, N. G. Parker, and C. F. Barenghi, Journal of Physics B: Atomic, Molecular and Optical Physics **47**, 095304 (2014).

[70] S. Nazarenko and M. Onorato, Journal of Low Temperature Physics **146**, 31 (2007).

[71] C. Rorai, K. R. Sreenivasan, and M. E. Fisher, Phys. Rev. B **88**, 134522 (2013).

[72] S. Prabhakar, R. P. Singh, S. Gautam, and D. Angom, Journal of Physics B: Atomic, Molecular and Optical Physics **46**, 125302 (2013).

[73] M. Leadbeater, T. Winiecki, D. C. Samuels, C. F. Barenghi, and C. S. Adams, Phys. Rev. Lett. **86**, 1410 (2001).

[74] S. Zuccher, M. Caliari, A. Baggaley, and C. Barenghi, Physics of Fluids **24**, 125108 (2012).

[75] A. T. Powis, S. J. Sammut, and T. P. Simula, Phys. Rev. Lett. **113**, 165303 (2014).

[76] W. J. Kwon, G. Moon, S. W. Seo, and Y. Shin, Phys. Rev. A **91**, 053615 (2015).

[77] W. J. Kwon, S. W. Seo, and Y. il Shin, *Periodic shedding of vortex dipoles from a moving penetrable obstacle in a bose-einstein condensate* (2015), `arXiv:1508.00958`.

[78] R. Desbuquois, L. Chomaz, T. Yefsah, J. Léonard, J. Beugnon, C. Weitenberg, and J. Dalibard, Nature Physics **8**, 645 (2012).

[79] G. W. Stagg, A. J. Allen, C. F. Barenghi, and N. G. Parker, Journal of Physics: Conference Series **594**, 012044 (2015).

[80] T. Winiecki and C. S. Adams, EPL (Europhysics Letters) **52**, 257 (2000).

[81] E. Hodby, G. Hechenblaikner, S. A. Hopkins, O. M. Maragò, and C. J. Foot, Phys. Rev. Lett. **88**, 010405 (2001).

[82] J. R. Abo-Shaeer, C. Raman, and W. Ketterle, Phys. Rev. Lett. **88**, 070409 (2002).

[83] J. E. Williams, E. Zaremba, B. Jackson, T. Nikuni, and A. Griffin, Phys. Rev. Lett. **88**, 070401 (2002).

[84] A. A. Penckwitt, R. J. Ballagh, and C. W. Gardiner, Phys. Rev. Lett. **89**, 260402 (2002).

[85] K. Kasamatsu, M. Tsubota, and M. Ueda, Phys. Rev. A **67**, 033610 (2003).

[86] C. Lobo, A. Sinatra, and Y. Castin, Phys. Rev. Lett. **92**, 020403 (2004).

[87] M. Leadbeater, T. Winiecki, and C. S. Adams, Journal of Physics B: Atomic, Molecular and Optical Physics **36**, L143 (2003), URL `http://stacks.iop.org/0953-4075/36/i=8/a=101`.

[88] M. Brewczyk, M. Gajda, and K. RzaÅijewski, Journal of Physics B: Atomic, Molecular and Optical Physics **40**, R1 (2007).

[89] N. P. Proukakis and B. Jackson, Journal of Physics B: Atomic, Molecular and Optical Physics **41**, 203002 (2008).

[90] N. Proukakis, S. Gardiner, M. Davis, and M. Szymanska, *Quantum Gases: Finite Temperatures and Non-equilibrium Dynamics*, Cold atoms (Imperial College Press, 2013), ISBN 9781848168107.

[91] P. Blakie, A. Bradley, M. Davis, R. Ballagh, and C. Gardiner, Advances in Physics **57**, 363 (2008).

[92] N. G. Berloff, M. Brachet, and N. P. Proukakis, Proceedings of the National Academy of Sciences **111**, 4675 (2014).

[93] Y. Kagan and B. V. Svistunov, Phys. Rev. Lett. **79**, 3331 (1997).

[94] M. J. Davis, S. A. Morgan, and K. Burnett, Phys. Rev. Lett. **87**, 160402 (2001).

[95] A. Sinatra, C. Lobo, and Y. Castin, Phys. Rev. Lett. **87**, 210404 (2001).

[96] N. G. Berloff and B. V. Svistunov, Phys. Rev. A **66**, 013603 (2002).

[97] M. J. Davis, S. A. Morgan, and K. Burnett, Phys. Rev. A **66**, 053618 (2002).

[98] C. Connaughton, C. Josserand, A. Picozzi, Y. Pomeau, and S. Rica, Phys. Rev. Lett. **95**, 263901 (2005).

[99] R. W. Pattinson, N. P. Proukakis, and N. G. Parker, Phys. Rev. A **90**, 033625 (2014).

[100] S. Nazarenko, M. Onorato, and D. Proment, Phys. Rev. A **90**, 013624 (2014).

[101] M. J. Davis and P. B. Blakie, Phys. Rev. Lett. **96**, 060404 (2006).

[102] T. M. Wright, N. P. Proukakis, and M. J. Davis, Phys. Rev. A **84**, 023608 (2011).

[103] T. P. Simula and P. B. Blakie, Phys. Rev. Lett. **96**, 020404 (2006).

[104] N. G. Berloff and A. J. Youd, Phys. Rev. Lett. **99**, 145301 (2007).

[105] N. Berloff and C. Yin, Journal of Low Temperature Physics **145**, 187 (2006), ISSN 0022-2291.

[106] H. Salman and N. G. Berloff, Physica D: Nonlinear Phenomena **238**, 1482 (2009), nonlinear Phenomena in Degenerate Quantum Gases.

[107] N. G. Berloff and B. V. Svistunov, Phys. Rev. A **66**, 013603 (2002).

[108] N. G. Berloff and P. H. Roberts, Journal of Physics A: Mathematical and General **34**, 10057 (2001).

[109] T. P. Simula, Phys. Rev. A **84**, 021603 (2011).

[110] W. Guo, M. La Mantia, D. P. Lathrop, and S. W. Van Sciver, Proceedings of the National Academy of Sciences **111**, 4653 (2014).

[111] S. N. Fisher, M. J. Jackson, Y. A. Sergeev, and V. Tsepelin, Proceedings of the National Academy of Sciences **111**, 4659 (2014).

[112] P. M. Walmsley and A. I. Golov, Phys. Rev. Lett. **100**, 245301 (2008).

[113] C. F. Barenghi, V. S. LâĂŹvov, and P.-E. Roche, Proceedings of the National Academy of Sciences **111**, 4683 (2014).

[114] P. M. Walmsley, P. A. Tompsett, D. E. Zmeev, and A. I. Golov, Phys. Rev. Lett. **113**, 125302 (2014).

[115] A. W. Baggaley, C. F. Barenghi, and Y. A. Sergeev, Phys. Rev. E **89**, 013002 (2014).

[116] D. V. Freilich, D. M. Bianchi, A. M. Kaufman, T. K. Langin, and D. S. Hall, Science **329**, 1182 (2010).

[117] L. Skrbek and W. Vinen, in *Quantum Turbulence*, edited by M. Tsubota and W. Halperin (Elsevier, 2009), vol. 16 of *Progress in Low Temperature Physics*, pp. 195 – 246.

[118] S. Davis, P. Hendry, and P. McClintock, Physica B: Condensed Matter **280**, 43 (2000).

[119] A. Guénault, V. Keith, C. Kennedy, S. Mussett, and G. Pickett, Journal of Low Temperature Physics **62**, 511 (1986), ISSN 0022-2291.

[120] D. Bradley, M. Človečko, M. Fear, S. Fisher, A. Guénault, R. Haley, C. Lawson, G. Pickett, R. Schanen, V. Tsepelin, et al., Journal of Low Temperature Physics **165**, 114 (2011).

[121] S. N. Fisher, A. J. Hale, A. M. Guénault, and G. R. Pickett, Phys. Rev. Lett. **86**, 244 (2001).

[122] R. Blaauwgeers, M. Blazkova, M. ÄŇloveÄŊko, V. Eltsov, R. de Graaf, J. Hosio, M. Krusius, D. Schmoranzer, W. Schoepe, L. Skrbek, et al., Journal of Low Temperature Physics **146**, 537 (2007).

[123] D. I. Bradley, M. Človečko, S. N. Fisher, D. Garg, E. Guise, R. P. Haley, O. Kolosov, G. R. Pickett, V. Tsepelin, D. Schmoranzer, et al., Phys. Rev. B **85**, 014501 (2012).

[124] J. Jäger, B. Schuderer, and W. Schoepe, Phys. Rev. Lett. **74**, 566 (1995).

[125] K. W. Schwarz, Phys. Rev. B **38**, 2398 (1988).

[126] R. Hänninen and A. W. Baggaley, Proceedings of the National Academy of Sciences **111**, 4667 (2014).

[127] R. Hänninen, M. Tsubota, and W. F. Vinen, Phys. Rev. B **75**, 064502 (2007).

[128] D. Kivotides, C. F. Barenghi, and Y. A. Sergeev, Phys. Rev. B **77**, 014527 (2008).

[129] K. W. Schwarz, Phys. Rev. Lett. **47**, 251 (1981).

[130] K. Henderson and C. Barenghi, Czechoslovak Journal of Physics **46**, 75 (1996), ISSN 0011-4626.

[131] J. Salort, P.-E. Roche, and E. Lévêque, EPL (Europhysics Letters) **94**, 24001 (2011).

[132] J. Salort, B. Chabaud, E. Lévêque, and P.-E. Roche, EPL (Europhysics Letters) **97**, 34006 (2012).

[133] P. Roberts and N. Berloff, in *Quantized Vortex Dynamics and Superfluid Turbulence*, edited by C. Barenghi, R. Donnelly, and W. Vinen (Springer Berlin Heidelberg, 2001), vol. 571 of *Lecture Notes in Physics*, pp. 235–257, ISBN 978-3-540-42226-6.

[134] G. W. Rayfield and F. Reif, Phys. Rev. **136**, A1194 (1964).

[135] A. Minguzzi, S. Succi, F. Toschi, M. Tosi, and P. Vignolo, Physics Reports **395**, 223 (2004).